Tandem reduction-reoxidation augments the catalytic activity of Sn-beta zeolites by redispersion and re-speciation of SnO_2 clusters.

Elise Peeters,[a] Ibrahim Khalil,[a] Pierre Eloy,[b] Sergio Calderon-Ardila,[a] Jan Dijkmans,[a] Paola Ferrini,[a] Damien P. Debecker,[b] Russell A. Taylor,[c] Alexios P. Douvalis,[d,e] Michiel Dusselier,[a] and Bert F. Sels*,[a]*

[a] Centre for Sustainable Catalysis and Engineering (CSCE), Leuven Chem&Tech, KU Leuven, Celestijnenlaan 200F, 3001 Heverlee, Belgium

[b] Institute of Condensed Matter and Nanosciences (IMCN), Université catholique de Louvain (UCLouvain), Place Louis Pasteur 1, Box L4.01.09, 1348 Louvain-La-Neuve, Belgium

[c]Department of Chemistry, Durham University, South Road, Durham DH1 3LE, UK

[d]Mössbauer Spectroscopy & Physics of Materials Laboratory, Department of Physics, University of Ioannina, 45110 Ioannina, Greece

[e]Institute of Materials Science and Computing, University Research Center of Ioannina (URCI), 45110 Ioannina, Greece

ABSTRACT

High dispersion of Sn in beta (β) zeolites is pivotal to obtain highly active Snβ catalysts with high productivity. However, at higher Sn loadings, Sn dispersion and the activity per Sn decrease. The

present work highlights the augmentation of catalytic activity in the Baeyer-Villiger oxidation and Meerwein-Ponndorf-Verley reactions of as-synthesized Snβ catalysts with Sn loadings up to 10 wt. % by tandem reduction-reoxidation and discusses the effect in terms of Lewis Acid (LA) density, Sn dispersion, Sn speciation, and catalytic performance. To do so, non-treated, reduced and reduced-reoxidized Snβ catalysts are characterized by N_2-physisorption, XRD and a multitude of spectroscopic techniques such as TPR-MS, probe FTIR, DRUV-vis, ^{119}Sn Mössbauer, ^{119}Sn MAS NMR, ICP-AES and XPS. Although not mutually exclusive, the higher catalytic activity seems to arise from different phenomena depending on the Sn loading. At lower Sn content (≤ 5 wt. %), the higher activity arises from redispersion of SnO_2 clusters into smaller active Sn species whereas at higher Sn content (≥ 5 wt. %), the catalytic activity seems to improve based on re-speciation of SnO_2 clusters.

INTRODUCTION

Lewis acidic Sn incorporated in a beta (β) zeolite is highly active in industrially relevant reactions such as the reduction of ketones/aldehydes to alcohols by Meerwein-Ponndorf-Verley reaction (MPV),[1–3] the oxidation of ketones to esters with H_2O_2 (Baeyer-Villiger oxidation, BVO),[4–8] the isomerization and epimerization of sugars,[9–18] the conversion of carbohydrates into lactic acid,[19–21] and aldol condensations.[22,23] There is general consensus that Snβ catalysts contain Lewis acidity (LA), but the exact structural properties of the active Sn site is still debated. Sn can be incorporated into the framework of the β zeolite and/or can be deposited as extra-framework Sn oxide clusters of varying size in- or outside the zeolite pores. Based on CD_3CN-FTIR and ^{119}Sn MAS NMR spectroscopy, closed and open framework Sn sites were suggested.[24,25] Closed sites (weak LA) are tetrahedrally coordinated to four zeolitic framework oxygen [*viz.* $Sn(OSi)_4$],

whereas open Sn sites (strong LA) are only coordinated to three zeolitic oxygens plus one extraframework hydroxyl group [*viz.* $Sn(OSi)_3(OH)$].[24] This assignment is inspired by the previously defined open and closed sites in TS-1 catalysts.[26,27] However, new evidence of active dimeric Ti-species challenges the widely accepted idea of isolated (open and closed) framework Ti sites.[28,29] Hence, grasping the full identity of the active Sn site(s) might be even more complicated than previously thought.

Evidence for the existence of the open Sn site remains ambiguous. Ivanova *et al.* could not detect any silanol group in the proximity of a dehydrated framework Sn site. Instead, they suggested that different Sn locations in the framework are at the basis of the different Lewis acidity.[30] Upon hydration, these strong LA Sn sites rapidly form hexacoordinated Sn (in a few hours at RT) via the dissociative adsorption of two water molecules.[30] In contrast, weak LA Sn sites show almost no interaction when a small amount of water is added[31] but at a higher water content, the weak LA Sn sites starts to interact with one H_2O-molecule forming a pentacoordinated Sn site, followed by a very slow rearrangement into the hexacoordinated state (up to 1 month at RT).[30] Numerous studies put forward the open or strong LA Sn sites as the only catalytically active sites for the BVO, MPV and sugar isomerization reaction.[15,24,32,33] However, recently, the closed or weak LA Sn sites were found to be also active in the MPV reaction,[34] and also small SnO_2 clusters, confined inside the pores, were found to catalyze BVO and glucose isomerization reactions.[35,36] Hence, instead of focusing solely on open/closed Sn sites, all Lewis acidic active Sn sites should be taken into consideration to describe and understand catalysis with Sn containing zeolites. In our latest paper, a linear correlation between BVO activity and total LA density (up to a LA density of 200 $\mu mol \cdot g^{-1}$) was found.[8] Such a linear relationship was also reported for cyclohexene oxide hydration and the glucose to methyl lactate reaction.[21,37] In general, a highly active Snβ catalyst exhibits a

high Sn dispersion (and thus a high amount of LA site density) and shows the absence of large inactive SnO_2 clusters (possessing insignificant LA density).

The nature of Sn species present (*i.e.,* framework Sn, small pore confined SnO_2 species and/or large inactive SnO_2 clusters) is dependent on the Snβ synthesis method. There are several ways to incorporate Sn cations into a zeolite such as a β material. The direct (fluoro-assisted[4,38] or hydroxyl-assisted[39]) hydrothermal (HT) crystallization forms Snβ crystals by treating a tin containing siliceous gel under hydrothermal conditions. The post-synthetic (PS) method involves the removal of framework Al by acid leaching to form vacancy framework defects followed by doping this defected zeolite with Sn via gas-phase chemical vapor deposition (CVD),[40,41] liquid-phase grafting[42,43] or solid-state incorporation.[44,45]

For CVD and grafting, it was previously suggested that the driving force for Sn incorporation is the surface reaction between framework Si-OH and Sn-Cl, forming HCl.[40,42] For solid-state incorporation, we recently corroborated that the Sn incorporation under inert heating (*i.e,* pre-pyrolysis) is driven by Sn(II)O species. Their higher volatility and hence mobility compared to $Sn(IV)O_2$ species significantly improved the Sn dispersion. These findings explained the higher BVO activity of the solid-state (SS) Sn-beta zeolites synthesized via preheating under inert atmosphere (pre-pyrolysis) compared to the one-step air-calcined method.[8]

With this knowledge in mind, we hypothesized that Sn dispersion, and hence the catalytic activity of (inferior) Snβ catalysts with high amounts of large extra-framework SnO_2, can be increased by high-temperature reduction of the extra-framework SnO_2 clusters to Sn(II)O species. After subsequent oxidation, these latter species can transform into active Sn(IV) sites (either as framework Sn or small SnO_2 clusters (< 2nm)). Reduced SnO_2 species have been studied frequently in the broader field of redox chemistry (*e.g.,* semiconductors, water splitting, and

batteries).[46,47] Yet, reports on Sn cation reduction in siliceous frameworks, and its relation with catalysis, are less common. In the mid '90s, scarce publications studied the reduction of Sn in mesoporous MCM-41 and microporous zeolite topologies, such as MWW and MEL. ^{119}Sn Mössbauer spectroscopy indicated that stable, firmly anchored framework Sn(II) species were formed upon reduction in H_2, which could then be reoxidized to Sn(IV) species.[48–50] In 2016, our group demonstrated the reduction of framework Sn(IV) to Sn(II) in a BEA zeolite topology under H_2 atmosphere.[51] Interestingly, a lower temperature was needed to reduce the Sn atoms in the materials made via PS grafting compared to HT synthesis, which was attributed to a weaker bonding of Sn to the zeolite support.[51] More recently, the group of Ivanova reported that reduction of Sn under hydrogen decreased the amount of framework Brønsted (Sn-OH--OH-Si) and Lewis acid sites in HT Snβ.[52] Apart from these results, no further in-depth characterization on such reduced Sn sites in β zeolites has been reported.

Hence, in this work we first perform a detailed characterization of reduced Sn species inside β zeolites with low and high Sn dispersion. Secondly, we investigate the effect of this reduction-oxidation strategy on the catalytic activity of a solid-state Snβ containing a high amount of large SnO_2 clusters in the BVO and MPV reaction. Finally, a link will be proposed between the type of Sn species formed and the catalytic activity of Snβ in both BVO and MVP reactions.

Results and discussion

Snβ samples with a significant amount of SnO_2 species (*i.e.,* low Sn dispersion of 30%) were reduced to investigate the possible redispersion of Sn from such extra-framework Sn oxide clusters. The Sn dispersion is calculated by dividing the total amount of active Sn sites, as determined by pyridine-FTIR (assuming one active Sn site per adsorbed molecule of Py) by the total amount of Sn atoms (calculated via ICP-AES, *vide infra*). Such low-dispersed Snβ starting

samples were made by solid-state (SS) stannation of dealuminated beta zeolites with Sn(II) acetate via air-calcination without a pre-pyrolysis step.[8] These Snβ samples were reduced and the resulting Sn species were characterized by powder X-ray diffraction (PXRD) and spectroscopy techniques including temperature-programmed reduction mass-spectroscopy (TPR-MS), ^{119}Sn Mössbauer, diffuse reflectance UV-vis (DRUV-vis) and Fourier Transform infrared spectroscopy (FTIR).

1. Reduction of Snβ zeolites: in-depth characterization of Sn species

TPR-MS was performed on the Snβ samples to investigate H_2 consumption as a function of temperature. In Figure 1A the TPR-MS data of an air-calcined SS Snβ (2 wt. % Sn; further denoted as 2Snβ-air) showed H_2 (m/z = 2) uptake between 450 and 1000 °C with a maximum at 600 °C. In Figure S1, the TPR results of 5Snβ-air and calcined dealuminated β zeolite (deAlβ-air) are also presented. Instead of one maximum, the 5Snβ-air shows two H_2-consumption maxima at 610 °C and 950 °C. DeAlβ-air showed marginal H_2-consumption and H_2O (m/z = 18) production starting from 500 °C (Figure S1B). The water probably originates from the formation of siloxane bridges by condensation of neighbouring silanols, which are present in large amounts in the form of silanol nests. However, water formed during the reduction of 2- and 5Snβ-air does not solely originate from silanol nest condensation since the temperature of the major peak coincides with the H_2 consumption maximum. Simultaneous H_2 consumption and H_2O production indicate that H_2 reacts with the framework Sn(IV) or SnO_2 species, thereby removing coordinating oxygen atoms in the form of water.

DRUV-vis spectroscopy was performed on dry 2Snβ-air samples that were reduced at 600, 700 and 900 °C. The electronic absorption spectra of these reduced samples as well as the non-reduced reference sample are displayed in Figure 1B. A new signal appeared after reduction, indicating a change in the electronic structure of Sn species in the reduced samples. The reference sample

showed a broad signal at 275 nm and a small signal at 210 nm, which can be ascribed to extra-framework SnO_2 and tetrahedrally coordinated Sn(IV) sites, respectively.[35,42] After reduction at 600 °C, the band at 275 nm disappeared together with the appearance of a new signal at 250 nm; this latter band was even more intense at 700 °C. This conversion coincides with H_2 consumption. At 900 °C, both bands at 210 and 250 nm, drastically decreased. Since TPR-MS data indicated the consumption of H_2 at 600-700 °C, the newfound signal (250 nm) was tentatively linked to reduced Sn species. Literature on this topic was consulted but found to be scarce. Some reports on nanocrystalline SnO indicate absorption signals of Sn(II) species around 250-270 nm.[53–55] Furthermore, reduction of Sn(IV) to Sn(II) causes an increase in ionic radius (0.69 to 1.18 Å)[56] related to the formation of a free electron pair with both s- and p-orbital character.[48] The s-to-p intershell electron transfers caused by UV absorption are typically located in the 250-300 nm range.[57] It is therefore plausible that the absorption band at 250 nm is related to Sn(II) ions in the zeolite framework.

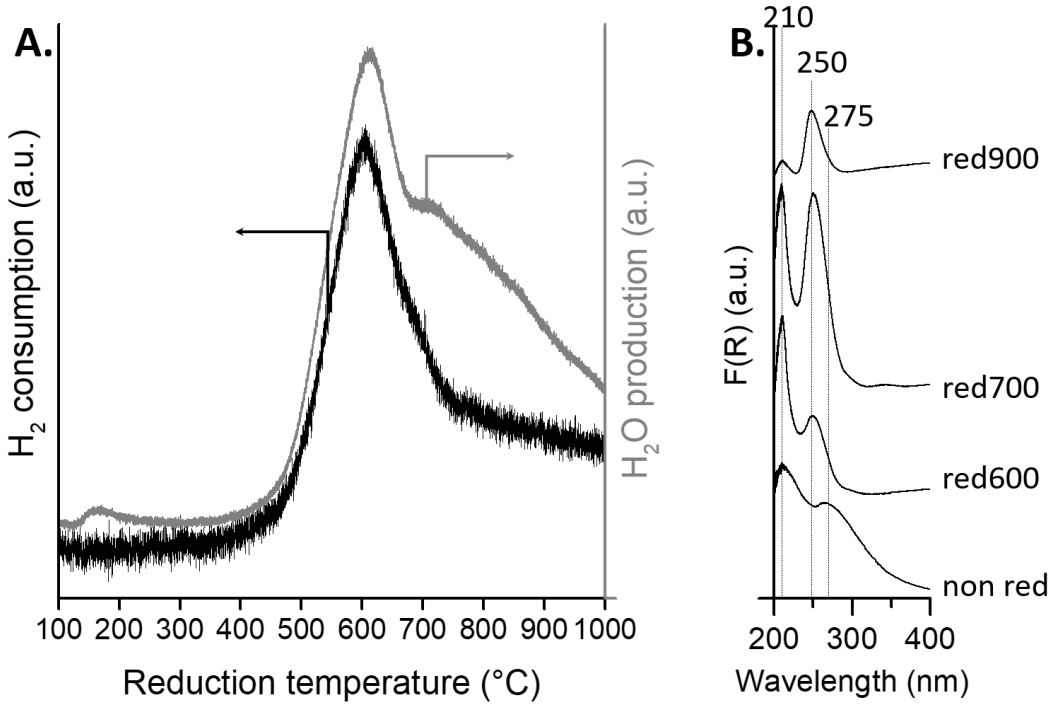


Figure 1. (**A**) Consumption of H_2 (black) and production of H_2O (grey) in solid-state 2Snβ-air as a function of temperature by TPR-MS under flowing H_2. (**B**) DRUV-vis spectra of 2Snβ-air non-reduced and reduced at 600, 700 and 900 °C under flowing H_2. Abbreviations: redX, reduced at X °C; non red, non-reduced 2Snβ-air.

Unambiguous proof of the formation of Sn(II) species by reducing Sn(IV) species with H_2 was provided by ^{119}Sn Mössbauer spectroscopy (Table 1). While all Sn in non-reduced 2Snβ-air is present as Sn(IV) (entry 1 and Figure S2A), 52% of Sn(II) and 31% of Sn(0) appeared in 2Snβ-air after reducing at 700 °C (*i.e.,* 2Snβ-air-red700) with 17% of Sn(IV) remaining (entry 7, Figure S2B). Further, 95% of Sn(IV) was reduced at 900 °C (entry 10) giving 25% of Sn(II) and more than double the amount of Sn(0) (70%). The further reduction towards metallic Sn at high reduction temperature can be seen by the second H_2-consumption maximum at 950 °C for 5Snβ-air (Figure S1), or the H_2-consumption values which are not returning to the initial values after 700 °C for 2SnSnβ-air.

Table 1. ^{119}Sn Mossbauer parameter values resulting from spectra recorded at 77 K of selected Snβ zeolites varying in Sn content, synthesis method, and reduction and reoxidation temperatures.

No.	Material[a]	Sn (wt.%)	IS [$Sn^{IV}/Sn^{II}/Sn^0$] ($mm \cdot s^{-1}$)	QS [$Sn^{IV}/Sn^{II}/Sn^0$] ($mm \cdot s^{-1}$)	AA [$Sn^{IV}/Sn^{II}/Sn^0$] (%)
	Non-reduced				
1[b]	2Snβ-air	1.6	0.02	0.52	100/0/0
2[b]	5Snβ-air	4.3	0.01	0.51	100/0/0
3[b]	10Snβ-air	9.5	0.03	0.54	100/0/0
4[b]	2Snβ-N_2/air	1.7	-0.10/3.16	0.65/1.84	94/6/0

5[b]	5Snβ-N_2/air	4.4	-0.08/3.01	0.70/1.49	96/4/0
6[b]	10Snβ-N_2/air	9.2	-0.06/3.01	0.75/2.16	97/3/0
	Reduced				
7	2Snβ-air-red700	1.6	-0.10/3.05/2.63	0.64/2.15/0.28	17/52/31
8	5Snβ-air-red700	4.3	-0.09/3.05/2.63	0.56/2.16/0.27	29/48/23
9	10Snβ-air-red700	9.5	-0.10/3.02/2.57	0.59/2.09/0.25	22/39/39
10	2Snβ-air-red900	1.6	-0.03/3.03/2.60	0.66/2.15/0.30	5/25/70
11	2Snβ-N_2/air-red700	1.7	-0.09/3.04/2.66	0.54/2.14/0.31	25/61/14
12	5Snβ-N_2/air-red700	4.4	-0.06/3.00/2.60	0.59/2.13/0.30	26/53/21
13	10Snβ-N_2/air-red700	9.2	-0.10/3.00/2.57	0.65/2.10/0.34	25/47/28
	Reduced – reoxidized				
14	2Snβ-air-red700-reox150	1.6	-0.12/3.13/2.59	0.61/2.04/0.26	54/15/28
15	2Snβ-air-red700-reox550	1.6	-0.08/2.96	0.57/1.12	94/6/0
16	10Snβ-air-red700-reox550	9.5	-0.01/2.98	0.51/1.04	95/5/0
17	2Snβ-N_2/air-red700-reox550	1.7	-0.11/3.05	0.68/2.26	93/6/0
18	5Snβ-N_2/air-red700-reox550	4.4	-0.07/3.13	0.62/1.83	92/8/0
19	10Snβ-N_2/air-red700-reox550	9.2	-0.08/2.94	0.53/1.79	93/7/0
	Grafted				
20	2Snβ-graft	2.3	-0.14	0.73	100/0/0
21	2Snβ-graft-red700	2.3	-0.06/3.00	0.54/2.14	31/69/0
22	2Snβ-graft-red700-reox550	2.3	-0.10/3.08	0.67/2.03	91/9/0
	SnO_2				
23	SnO_2	-	0.04	0.51	100/0/0

[a] General material nomenclature: XSnβ-Y-redZ-reoxW = Snβ zeolite with X wt. % of Sn, synthesized via post-synthetic method Y (air: solid-state stannation via air-calcination, N_2/air:

solid-state stannation with pre-pyrolysis under N_2 prior to air-calcination, graft: liquid-state grafting) and reduced (in H_2) and reoxidized (in air) at temperature Z and W °C, respectively. [b] Previously published data from Peeters *et al*., 2021.[8], reprinted with permission, copyright (2021) American Chemical Society. Abbreviations: IS = isomer shift; QS = quadrupole splitting; AA = absorption area.

The formation of metallic Sn(0) was also confirmed by PXRD, which showed that Sn(0) is already formed at a reduction temperature of 600 °C (Figure S3). At higher Sn content (5 and 10 wt. %), Snβ-air samples displayed signature Bragg diffractions of SnO_2 which upon reduction disappeared. It thus seems that reduction in H_2 converts the initial, large SnO_2 clusters (as detected by PXRD) to Sn(II) or Sn(0) species (as measured by ^{119}Sn Mössbauer spectroscopy).

To investigate the influence of extra-framework Sn oxide clusters on the formation of metallic Sn, we compared the ^{119}Sn Mössbauer data of 2Snβ-air (Figure S2A and B) with 2Snβ-N_2/air (Figure S2C and D). This latter catalyst, made via two-step pre-pyrolysis/air-calcination, was previously shown to possess higher Sn dispersion relative to the corresponding one-step air calcination catalyst (58% *vs*. 20%)[8], and hence less extra-framework Sn oxide clusters because of an improved incorporation of Sn into the framework. Under identical reduction at 700 °C, it was found that for the sample with lower Sn dispersion (single-step calcination), not only more Sn(IV) is reduced (83% *vs*. 75%), but also more metallic Sn is formed (31% *vs.* 14%). This suggests that framework Sn(IV) is more resistant towards reduction to Sn(II) and metallic Sn, probably because of the stronger interaction of the tetrahedral framework Sn with the zeolite support. When comparing the reduction at 700 °C of 10Snβ-air containing large SnO_2 clusters (as detected by PXRD, Figure S3) against 10Snβ-N_2/air, with only small Sn(II)O clusters, it is seen that more metallic Sn is present when starting with large SnO_2 clusters (39% vs. 28%, Table 1 entries 9 and 13). Hence, larger SnO_2 clusters are more easily reduced towards metallic Sn compared to smaller

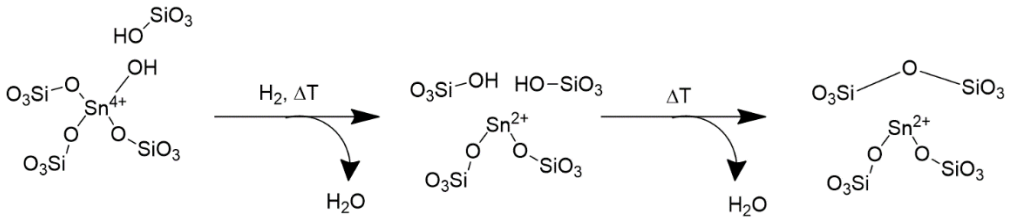
Sn oxides, which can also be rationalized by the better interaction of small SnO_2 clusters (containing more defects compared to large SnO_2) with the zeolite lattice.

The higher resistance of framework Sn towards reduction can also be deduced from the difference in the isomer shift (IS).[8,49] The IS value of Sn is affected by the contributions of *p* and *s* electrons; an increase in the contribution of *p* symmetry electrons decreases the IS value.[49] As tetrahedral bonding requires a larger contribution from *p* electrons compared to octahedral Sn in SnO_2, the tetrahedral framework Sn sites will possess lower IS values relative to the octahedral SnO_2 sites.[49,58,59] For the samples studied here, the Sn(IV) envelope of their Mössbauer spectra contains both contributions, but due to the relative low QS values, the Sn(IV) species are difficult to be distinguished (deconvoluted in the fittings), so they are modelled by a single component acquiring the average IS value of these contributions. However, an increase in the amount of tetrahedral framework Sn sites will shift the IS of the Sn(IV) component towards lower average values. This is indeed observed for the IS values of the two-step calcination process (N_2/air) samples compared to the single air step counterparts (Table 1, entries 4-6), and a higher negative IS shift is observed for the 2 wt. % sample, reflecting the higher incorporation of tetrahedral framework Sn sites in samples with low Sn loading.[49,58] Moreover, tetrahedral framework Sn sites also increase the QS values compared to the octahedral SnO_2 species. Hence, relatively higher QS values for the two-step calcination process sample indicate an increase in the distortion of the Sn(IV) environment for these sites.

Upon reducing the Sn(IV) ions in the 2, 5 and 10 wt. % Snβ-air samples (Table 1, entries 7-9), in each case the IS value of the remnant Sn(IV) lowered from approximately 0.02 to -0.10 $mm \cdot s^{-1}$, while for the two-step Snβ-N_2/air samples, the same Sn(IV) IS values were retained (Table 1, entries 11-13). This confirms that more framework Sn(IV) is present in the two-step calcination

process, and after reduction the majority of non-reduced Sn(IV) is tetrahedrally coordinated. Hence, octahedrally coordinated SnO_2 is more easily reduced towards Sn(II) and Sn(0).

We further investigated the higher resistance of framework Sn towards reduction to metallic Sn by reducing a Snβ with a high amount of framework Sn. To do so, we synthesized a Snβ of 2 wt. % via the grafting synthesis method.[43] Indeed, a Sn dispersion of 94% was obtained (calculated via Py-FTIR and ICP, results not shown). The IS and QS values of -0.14 and 0.73 $mm \cdot s^{-1}$ (Table 1, entry 20), respectively, correspond to a high framework Sn incorporation and agree with the high Sn dispersion. Upon reduction at 700 °C, indeed no Sn(0) is formed. Instead, 69% is present as Sn(II) and 31 % remains present as Sn(IV) (Table 1, entry 21). A tentative pathway for framework Sn reduction is proposed in Scheme 1.



Scheme 1. Proposed pathway for the reduction of tetrahedrally coordinated open Sn sites.

Overall, by reducing Snβ samples containing a significant amount of SnO_2 species, we identified both Sn(II) species and metallic Sn. TPR-MS, XRD, DRUV-vis and ^{119}Sn Mossbauer spectroscopy results suggested that tetrahedral framework Sn(IV) species are more resistant to reduction compared to SnO_2 clusters and once reduced to Sn(II), it will not further reduce towards metallic Sn. Moreover, these results showed that large SnO_2 clusters (detectable with XRD) undergo more easily a full reduction towards metallic Sn compared to small SnO_2 clusters. In the next section, we evaluate the effect of the formation of mobile Sn(II)O species by reduction on the catalytic activity.

2. Reoxidation of reduced Snβ zeolites: catalytic activity

2.1. Baeyer-Villiger oxidation (BVO) reaction

In the BVO of cyclohexanone (CHO) to ε-caprolactone (CL), Lewis acidic Sn activates the carbonyl of CHO, forming CL through a Criegee intermediate with H_2O_2.[4] To explore if reduction prompts higher Sn dispersion, subsequent reoxidation is necessary to increase the overall LA density, and hence the overall catalytic activity, since Sn(IV) is a stronger Lewis acid than Sn(II) and Sn(0).[52]

To do so, we first determined the optimal set of reduction and reoxidation temperatures by measuring the catalytic activity – calculated as the initial formation rate of CL ($r_{0,CL}$) (see materials and methods and Figure S4) – of 5Snβ-air in function of varying reduction (Figure 2A) and reoxidation temperature (Figure 2B). The optimal reoxidation temperature after reduction at 700 °C was 550 °C (Figure 2B, a catalytic activity increase from 54 to 89 mM_{CL} h^{-1}) and at higher oxidation temperatures, no further increase was observed. Hence, in Figure 2A all reduced samples are first reoxidized for 2 h at 550 °C prior to catalytic tests. The highest catalytic activity (89 $mM_{CL} \cdot h^{-1}$) was seen for samples that were reduced at 700 °C under H_2-flow for 2 h, *viz*. 5Snβ-air-red700-reox550 (Figure 2A). A relative increase in catalytic activity of 177% could be acquired for 5Snβ-air-red700-reox550 (89 $mM_{CL} \cdot h^{-1}$) compared to 5Snβ-air (32 $mM_{CL} \cdot h^{-1}$). The catalytic activity significantly dropped upon increasing the reduction temperature to 900 °C. This drop can be due to the aggregation of metal clusters into metal nanoparticles, leading to a decrease in Sn dispersion and hence catalytic activity.[60] The intact β topology observed at 900 °C by PXRD data (Figure S3) confirms that the decrease in the activity is not due to framework collapse. Finally, to exclude that the observed increase in catalytic activity for the treated catalysts is just a temperature-induced phenomenon, a reaction was performed with a 5Snβ-air sample calcined at 700 °C under

flowing air and a 5Snβ-air dried in an N_2-flow at 700 °C. Activities similar to 5Snβ-air were obtained (30.1 and 32.5 $mM_{CL} \cdot h^{-1}$, respectively), indicating the critical role of H_2 pre-reduction in promoting the catalytic activity.

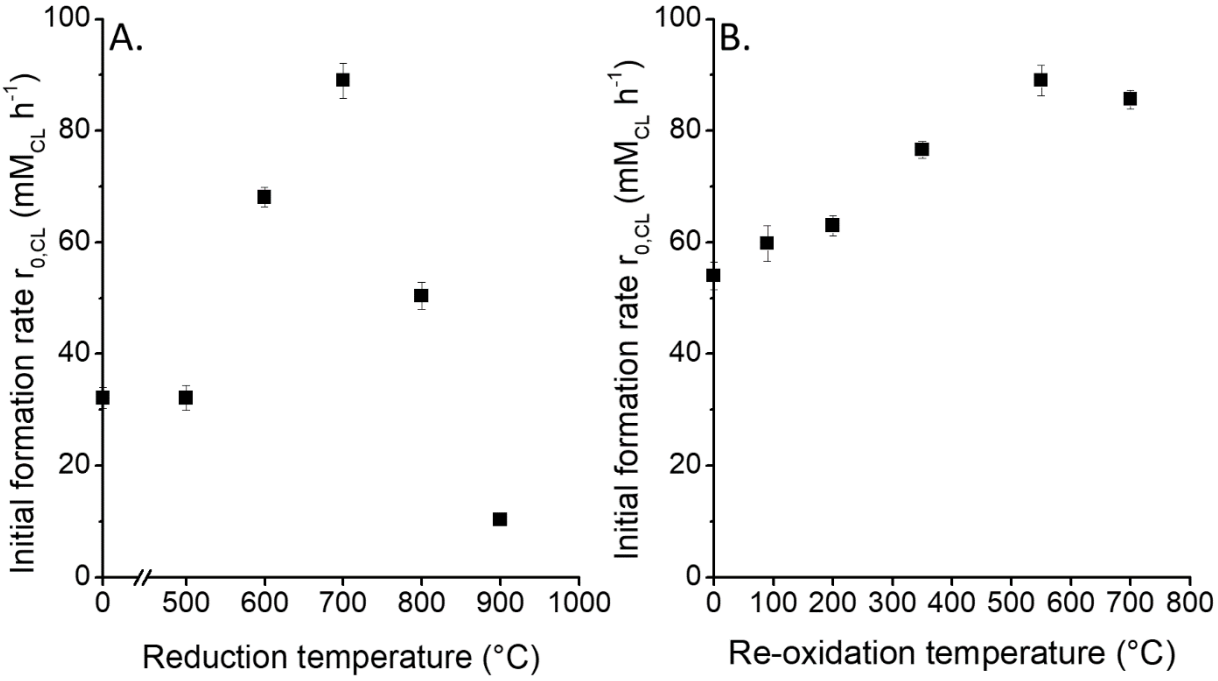


Figure 2. Catalytic activity for reduced - reoxidized 5Snβ-air catalysts. (**A**) Influence of reduction temperature (Z) for 5Snβ-air-redZ-reox550 samples. (**B**) Influence of reoxidation temperature (W) for 5Snβ-air-red700-reoxW samples. XSnβ-Y-redZ-reoxW = Snβ zeolite with X wt. % of Sn, synthesized via post-synthetic method Y (air or N_2/air) and reduced (in H_2) and reoxidized (in air) at temperature Z and W °C for 2 h, respectively. The point at 0 °C means that the catalyst is not reduced (2A) or no reoxidation is performed after reduction at 700 °C (2B). Reaction conditions: ketone (330 mM), 50 wt % H_2O_2 (H_2O_2/ketone = 1.5), 10 mg catalyst, 80 °C, 700 rpm.

In our previous work, the effect of the inert heat treatment step (pre-pyrolysis) on the catalytic BVO activity of the solid state Snβ samples and LA density was reported. It was seen that via a pre-pyrolysis step (abbreviated as N_2/Air), an increased catalytic activity and LA density was

obtained for the same Sn content as the air-calcined catalyst due to the presence of mobile Sn(II)O species instead of less volatile SnO_2 species (Figure 3, grey symbols).[8] To investigate if the reduction-reoxidation step increases the catalytic activity, all Snβ-(N_2/)air catalysts are reduced and reoxidized at the optimal temperatures, *i.e.* reduction at 700 °C in H_2-flow and a reoxidation at 550 °C in air-flow (denoted as redreox). No change in Sn content (in wt. %) was detected via ICP-AES after the reduction-reoxidation cycle (Table 1). For clarity, Table S1 provides a general overview of the main catalysts, the catalytic reactions and the applied characterization techniques.

Figure 3 plots the initial CL formation rate against Sn content for Snβ-air and Snβ-N_2/air samples before (in grey) and after optimal redreox (in orange and blue) and shows the influence of such a treatment on the catalytic BVO activity of samples made via the one- and two-step calcination method. Independent of Sn content, the catalytic activity of Snβ-air samples significantly improved after reduction-reoxidation. Up to a Sn content of 5 wt. %, the $r_{0,CL}$ of the treated Snβ-air samples even coincided with the untreated Snβ-N_2/air samples. These observations seem to suggest that it is indeed possible to redisperse (inactive) extra-framework SnO_2 through formation of intermediate mobile Sn(II)O species via reduction with H_2. In contrast, no additional BVO activity was obtained for treated Snβ-N_2/air samples with a Sn content up to 5 wt. %. Here it seems that the inert pretreatment step during solid-state exchange is already sufficient to create highly active Snβ catalysts as this preheating step in inert atmosphere already enables sufficiently high Sn dispersion.

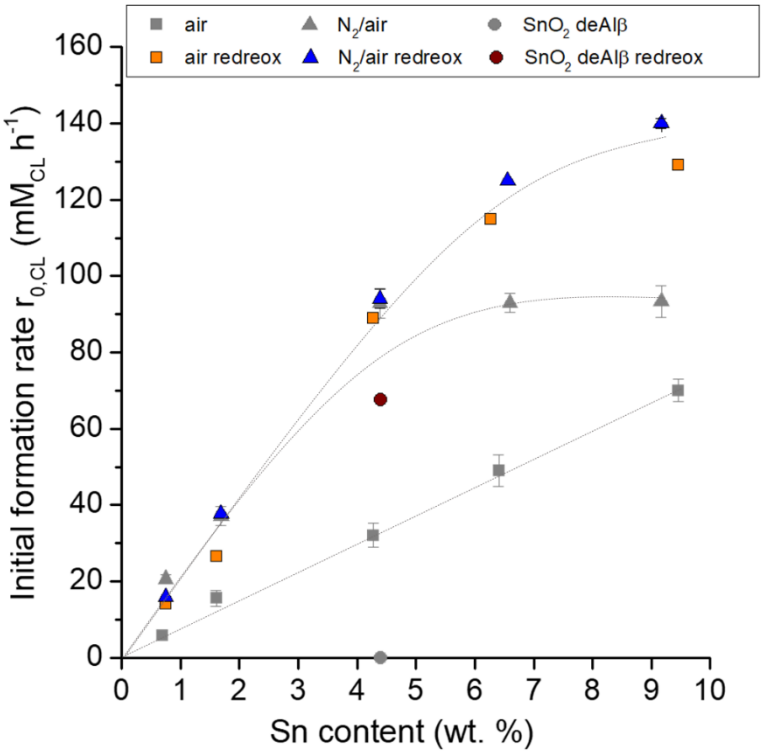


Figure 3. The initial formation rate of ε-caprolactone (CL) as a function of Sn content (wt.%) for the BVO of cyclohexanone with 50 wt.% H_2O_2 at 80 °C (reaction conditions: see Figure 2). Sn content was quantified by ICP-AES. Redreox = reduced at 700 °C in H_2-flow for 2 h and reoxidized at 550 °C in an air-flow for 2 h. The error bars represent the standard deviation of reactions performed in triplicate. The gray series were reported in our previous publication (ref 8.) and reprinted with permission, copyright (2021) American Chemical Society.

Interestingly, at higher Sn content (≥ 5 wt.%), the $r_{0,CL}$ of treated Snβ-N_2/air samples improved and even outperformed its untreated counterparts. This way, a maximum activity of 140 $mM_{CL} \cdot h^{-1}$ is obtained for 10Snβ-N_2/air-redreox compared to the plateau value of 93 $mM_{CL} \cdot h^{-1}$ for untreated Snβ-N_2/air catalysts. Hence, treatment of Snβ-(N_2/)air samples by reduction-reoxidation allows to surpass the activity plateau observed for Snβ-N_2/air samples. For instance, reduction-reoxidation

of 10Snβ-air and 10Snβ-N_2/air gives a relative increase in BVO activity of 85% and 50%, respectively.

In addition, to test our hypothesis that reduction redisperses (inactive) extra-framework SnO_2 through formation of mobile Sn(II)O species, we synthesized a solid-state Snβ sample with SnO_2 (abbreviated as SnO_2 deAlβ). The synthesis was performed via identical procedure as the solid-state Snβ-air samples (via grinding and air-calcination), but instead of Sn(II) acetate, SnO_2 is used as Sn precursor as it is a cheap and carbon-free alternative. However, in literature it is reported that SnO_2 as precursor gives inactive Snβ catalysts containing high amount of SnO_2 clusters.[8,37] Figure 3 shows that untreated 5SnO_2 deAlβ indeed did not possess any catalytic activity, which is in agreement with literature. After the reduction-reoxidation cycle, the 5SnO_2 deAlβ samples reaches 63 $mM_{CL} \cdot h^{-1}$, exceeding the 5Snβ-air catalyst made with Sn(II) acetate and supporting our hypothesis.

2.2. Meerwein-Ponndorf-Verley (MPV) reaction

Next, we investigated the effect of reduction-reoxidation on the catalytic activity for another well-studied Snβ catalyzed reaction, *i.e.*, the MPV reaction. The MPV reaction reduces an aldehyde or ketone to an alcohol in the presence of a sacrificial alcohol as the hydrogen donor (usually a secondary alcohol). The hydride transfer is facilitated by activating the carbonyl group with Lewis acidic Sn sites which makes the carbon atom of the carbonyl group more electrophilic.[1,2,33] Here, the MPV reduction of CHO with 2-butanol to cyclohexanol (CHOL) and 2-butanone is used as a model reaction. The effect of reduction-reoxidation was investigated by using the most active catalysts, *i.e.,* 10Snβ-(N_2/)air-redreox and their untreated counterparts. The specific reaction conditions are mentioned in materials and methods.

The kinetic plots of the MPV reaction are shown in Figure S5. The treated catalysts outperformed the untreated Snβ-(N_2/)air catalysts. To exclude that the change in activity are temperature-induced phenomena, Figure S5 also displays the catalytic activities of Snβ catalysts calcined at 700 °C, which were comparable to the ones calcined at 550 °C. In 2020, Deng *et al*. reported a decrease in MPV activity upon dehydration of Snβ catalysts at 120 °C as the amount of active open Sn sites decreased.[61] However, in this case, the catalytic activity of our (un)treated catalysts was not measured instantly, but after storing them under ambient conditions for at least two days.

2.3 Kinetic catalysts parameters for BVO and MPV reactions

The increased BVO and MPV activity of reduction-reoxidation catalysts prompted us to further scrutinize the active Sn species involved. To do so, we performed kinetic studies to obtain and compare the kinetic parameters such as the apparent activation energy (E_a) and the pre-exponential factor (k_0). The Arrhenius plots are displayed in Figure S6 and the apparent E_a values were obtained from the slopes of these plots (measurements performed between 50-80 °C) whereas k_0 values were derived from the calculated intercept with the y-axis. E_a and k_0 values are listed in Table 2. For all reactions, it seems that upon reduction-reoxidation, the E_a values stay very similar. The E_a values of the MPV and BVO reaction are comparable to the one reported for HT Snβ (63 kJ·mol^{-1}),[33] and BVO PS SS Snβ (70 kJ·mol^{-1})[8], respectively. Moreover, these E_a-values indicate that all reactions were performed in absence of mass transfer limitations. According to the Eyring analysis,[62] a similar activation energy means that during the reaction a transition state with similar enthalpic level is formed at the Sn active sites of the reduced materials. The pre-exponential factor k_0 is influenced by the entropic factors and/or change in amount of active sites. For both the BVO and MPV reaction, k_0 increases after the reduction-reoxidation reaction by approximately a factor

2. Thus, it seems that the active site surroundings in the treated catalysts more efficiently accommodate the required substrate orientation and/or that the number of active sites increases after the reduction reoxidation cycle. This will be further discussed in the discussion section after measuring the number of active sites for the various catalysts (*vide infra*).

Table 2. Apparent activation energy (E_a) and pre-exponential factor (k_0) of the (un)treated 10Snβ-(N_2/)air catalysts for the BVO and MPV reactions.

Catalyst	**BVO**		**MPV**	
	E_a $(kJ \cdot mol^{-1})$	k_0 (h^{-1})	E_a $(kJ \cdot mol^{-1})$	k_0 (h^{-1})
10Snβ-air	70.1	$4.5\ 10^9$	62.7	$4.2\ 10^8$
10Snβ-air-redreox	70.3	$8.5\ 10^9$	63.8	$1.2\ 10^9$
10Snβ-N_2/air	70.6	$7.4\ 10^9$	64.0	$1.1\ 10^9$
10Snβ-N_2/air-redreox	71.8	$1.5\ 10^{10}$	66.2	$3.4\ 10^9$

3. Reoxidation of reduced Snβ-zeolite: characterization

If the Sn redispersion hypothesis indeed explains the increased catalytic (BVO and MPV) activity after tandem reduction-reoxidation, we would expect the LA density, and hence the Sn dispersion to increase after this reduction-reoxidation step (i) for Snβ-air catalysts over the whole Sn content range, and (ii) for Snβ-N_2/air catalysts, at a Sn content higher than 5 wt. %.

3.1 Pyridine and CD_3CN FTIR

The LA density was probed via Py-FTIR (see materials and methods). Figure 4A shows the LA density as a function of Sn content for the two calcination methods treated with and without tandem reduction-reoxidation. For the Snβ-air samples, the treatment increased the LA density over the whole Sn content range, and up to 5 wt. % of Sn, the LA densities corresponded to the values of Snβ-N_2/air. In contrast, for treated Snβ-N_2/air samples with up to 5 wt. % of Sn, the LA density remained unchanged. So far, these trends match the catalytic activity data, hence supporting the redispersion hypothesis. However, for both Snβ-air and Snβ-N_2/air at higher Sn loadings (> 5 wt. %) the LA density trend started to deviate from the catalytic activity trend. Whereas the activity kept increasing (Figure 3), the LA density hovered around 200 $\mu mol \cdot g^{-1}$.

This can also be expressed in terms of Sn dispersion. Figure S7 depicts the Sn dispersion against Sn content by assuming one adsorbed pyridine molecule per active Sn site.[63] Because of the treatment, the Sn dispersion of Snβ-air samples increased from 20-30% to 60% at low Sn loadings. For the N_2/air-catalysts with up to 5 wt. % of Sn, similar Sn dispersion appeared after the treatment, but at high Sn loadings, the dispersion dropped below the dispersion of the non-treated samples.

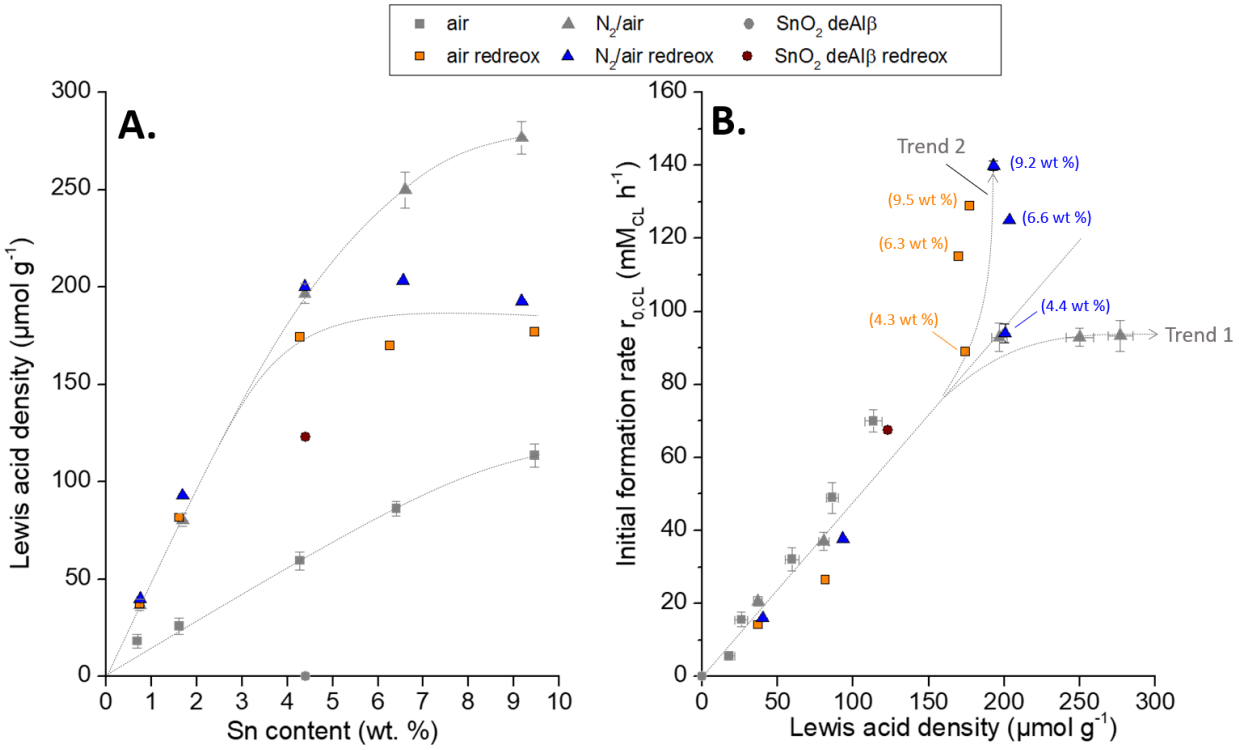


Figure 4. A. Influence of the redreox step on the Lewis acid density of Snβ-(N_2/)air and SnO_2-deAlβ with varying Sn content. **B.** Catalytic activity against Lewis acid density for the BV oxidation of CHO with 50 wt. % H_2O_2 at 80 °C (reaction conditions: see Figure 2). For clarity, the Sn content in wt. % is mentioned for the redreox samples at high Sn loading. The Lewis acid density was calculated by Py-FTIR at 150 °C and 1.42 cm.µmol^{-1} as integrated molar extinction coefficient.[63] The gray series were reported in our previous publication (ref 8.) and reprinted with permission, copyright (2021) American Chemical Society. Abbreviations: redreox, reduced at 700 °C in H_2-flow for 2 h and reoxidized at 550 °C in an air-flow for 2 h. Reproducibility was checked by performing Pyridine-FTIR spectroscopy and the BVO reaction for some catalysts in duplicate and triplicate, respectively. Error bars represent the standard deviations.

The LA density of SnO_2 deAlβ (5 wt. % Sn) before and after treatment are also presented in Figure 4A. Initially, the material possessed insignificant LA density which agrees with the absence

of catalytic activity (Figure 3) and after treatment, the LA density of 5SnO_2 deAlβ increased to 123 μmol·g^{-1}. This demonstrates that out of large SnO_2 clusters (see XRD below), active sites can be created by redispersion of the Sn species with the reduction-reoxidation step.

Figure 4B plots the catalytic BVO activity against the LA density before and after tandem reduction-reoxidation. At lower values, irrespective of the calcination method (air or N_2/air) and Sn precursor (Sn(II) acetate or SnO_2) used, a clear linear correlation is seen between the catalytic activity (< 93 mMCL·h^{-1}) and the LA density (< 200 μmol·g^{-1}). However, at higher values, two trends become apparent. Firstly, the catalytic activity stabilized (at 93 mM_{CL}·h^{-1}) while the LA density further increased (up to 275 μmol·g^{-1}) for non-treated (Snβ-N_2/air) samples (Trend 1). Secondly, the catalytic activity increased (up to 140 mM_{CL}·h^{-1}) while the LA density stabilized (at approximately 200 μmol·g^{-1}) for treated (Snβ-air and Snβ-N_2/air) samples (Trend 2).

As previously discussed by our group, the plateau in catalytic activity (Trend 1) was suggested to be due to Sn incorporation in less favourable sites at high Sn loadings.[8] However, the plateau in LA density (Trend 2) arising after the tandem reduction-reoxidation was not previously observed. One possible explanation might be that the LA sites are more accessible for reaction since the harsh reduction conditions created a more open pore structure (*e.g.*, hierarchization). However, the pore structure was not altered significantly by the treatment as confirmed by the similar pore volumes measured via N_2-physisorption (Table S2). Moreover, the E_a values (Table 2) indicated that the reactions took place in absence of mass transfer limitations.

The levelling off in LA density is also not due to the presence of more metallic Sn and Sn(II) species (with lower Lewis acidity) at high Sn loading. Reoxidation at 550 °C indeed converted almost all Sn(II) and Sn(0) back into Sn(IV) for all Sn loadings, as evidenced by the ^{119}Sn Mössbauer data, with only 5-8% of Sn(II) remaining (Table 1, entry 15-19). Note that at a

reoxidation temperature of 150 °C, only a third of the Sn(II) is reoxidized into Sn(IV) while almost all Sn(0) remained (Table 1, entry 14). Hence, this explains the lower catalytic activity at low reoxidation temperatures (Figure 2B).

Another explanation might be the underestimation of active sites with pyridine as a probe molecule. Therefore, we also tested the smaller acetonitrile-d_3 (CD_3CN) probe. CD_3CN preferentially adsorbs on strong LA Sn sites (2316 cm^{-1}) prior to coordinating to weaker LA Sn sites (2308 cm^{-1}). At higher coverage, CD_3CN adsorbs at SiOH groups (2275 cm^{-1}) and large non-framework SnO_2 groups (2290 cm^{-1}). Finally, at full saturation, physisorbed CD_3CN appears (2265 cm^{-1}).[52,63] After saturation, a spectrum was taken after 30s vacuum to remove physisorbed CD_3CN and this was deconvoluted into the principal bands (Figure S8). The total amount of Sn sites was estimated by combining the strong LA Sn sites with the weak LA Sn sites (see materials and methods). A similar amount of LA sites (within experimental error) was obtained when titrating with pyridine or CD_3CN (Figure 5A). CD_3CN can also be used to distinguish between strong and weak LA Sn sites. While weak LA Sn sites drastically decreased at high Sn loading (≥ 5 wt. %, Figure 5B) after treatment compared to the N_2/air-catalysts, the amount of strong LA Sn sites is similar to the untreated N_2/air counterparts (Figure 5C).

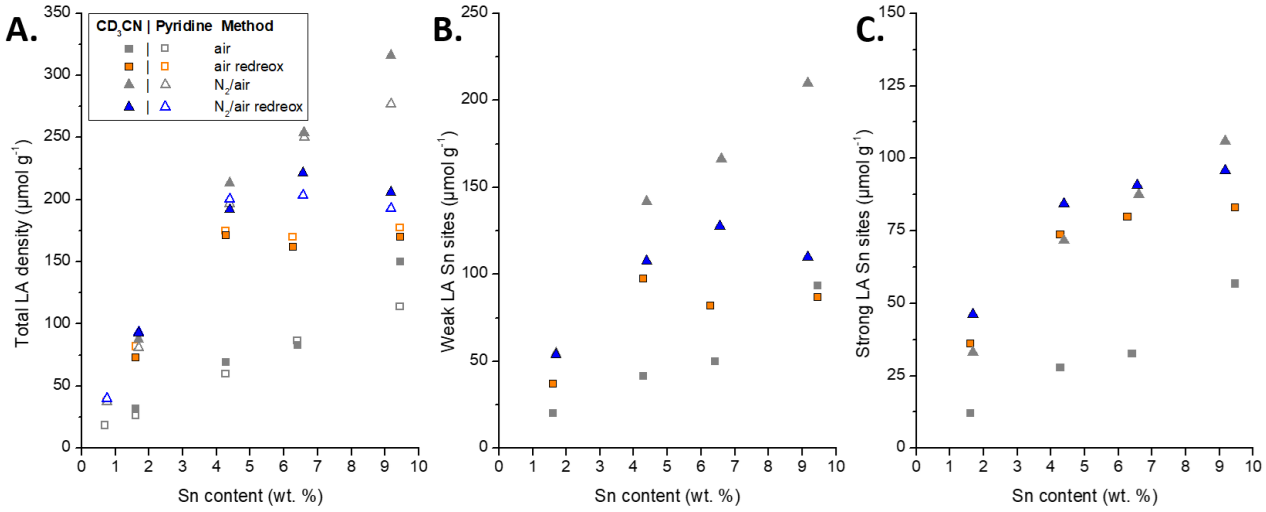


Figure 5. A. Total **B.** weak and **C.** strong LA Sn sites against Sn content. Via Py-FTIR, LA density was measured at 150 °C, and calculated with an integrated molar extinction coefficient (ε) of 1.42 cm·µmol^{-1}.[63] Via CD_3CN-FTIR, LA density was measured at 30 °C, 1.04 and 2.04 cm·µmol^{-1} were used as ε-values for strong LA (or open) and weak LA (or closed) Sn sites, respectively.[63] The gray series were reported in our previous publication (ref 8.) and reprinted with permission, copyright (2021) American Chemical Society. Abbreviations redreox: reduced (in H_2) at 700 °C and reoxidized (in air) at 550 °C.

When plotting the activity against either weak or strong LA Sn sites (Figure 6 A and B), a linear correlation can be noticed for the treated catalysts in terms of strong LA Sn sites, also at high Sn loadings. Hence, even though the number of strong sites is similar to the non-treated N_2/air-catalysts (at Sn ≥ 5 wt. %, Figure 5C), the strong Sn species are becoming more active. Therefore, in contrast to the Sn redispersion at lower Sn loadings, it is hypothesized that more active Sn species are formed (Sn re-speciation) at higher Sn loadings after tandem reduction-reoxidation.

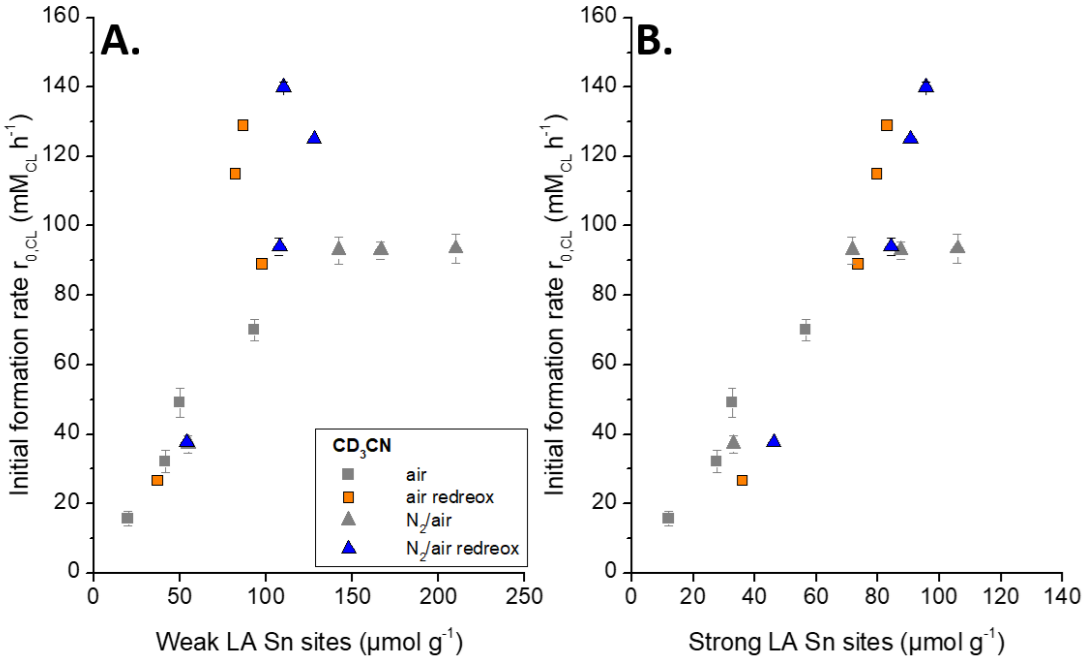


Figure 6. Initial formation rate against **A.** weak and **B.** strong LA Sn sites. LA density was measured via CD_3CN FTIR at 30 °C, 1.04 and 2.04 $cm \cdot \mu mol^{-1}$ were used as ε-values for strong LA (or open) and weak LA (or closed) Sn sites, respectively.[63] The gray series were reported in our previous publication (ref 8.) and reprinted with permission, copyright (2021) American Chemical Society. Abbreviations redreox: reduced (in H_2) at 700 °C and reoxidized (in air) at 550 °C.

3.2 SS NMR, XRD, ICP/XPS and ^{119}Sn Mössbauer spectroscopy

To characterize the Sn species present at high Sn loadings, solid-state ^{119}Sn NMR with Carr-Purcell-Meiboom-Gill (CPMG) echo-train acquisition under MAS was performed on 10Snβ-N_2/air samples before and after treatment. CPMG acquisition significantly reduces the acquisition time which enables data acquisition at natural abundance levels of ^{119}Sn.[64,65] In general, solid-state ^{119}Sn MAS NMR can be used to differentiate extra-framework SnO_2 and framework Sn(IV) species, and more specifically it can make a distinction between strong and weak LA framework Sn sites.[25,30,66] Figure 7A shows the cross polarization (CP-CPMG) spectra acquired for the hydrated 10Snβ-N_2/air samples with and without tandem reduction-reoxidation. The hydrated samples gave a broad signal with peak maxima at -651 (non-treated) and -660 ppm (treated), respectively. Chemical shifts between -650 and -700 ppm are typically assigned to hydrated framework Sn sites. The exact chemical shift of these octahedrally coordinated species depends on multiple factors including the T-site, number of proximal defects and Sn content.[67–69]

In the direct excitation (DE-CPMG) spectra of the dehydrated catalysts (Figure 7B), the dehydrated sample before treatment showed signals for strong (-425 ppm) and weak (-442 ppm) tetrahedral Sn sites, while no signal for octahedral SnO_2 (-600 ppm) was detected. In contrast, after treatment, the dehydrated sample gave a dominant signal at -600 ppm, while the intensities of the

signals at -425 and -450 ppm were strongly reduced. The latter is in sharp contrast with the CD_3CN-FTIR data, which indicated almost no change in the amount of strong LA Sn sites (Fig. 5C). Moreover, three additional Sn signals appeared at -512, -543 and -574 ppm. These were excluded to be spinning sidebands of SnO_2, since no mirrored signals were seen around the main SnO_2 resonance. According to literature, these signals could be indicative of pentacoordinated Sn species.[30,31,67,69] It has been reported that for hydrated Snβ zeolites, weak LA Sn sites initially form pentacoordinated Sn species, while, strong LA Sn sites interact with two water molecules forming a hexacoordinated Sn site. Ivanova *et al.* reported that in presence of a large amount of water (H_2O/Sn = 4), they could not detect an intermediate pentacoordinated Sn site for strong LA Sn sites, probably because it reacted faster than the time scale of the experiment (first measurement after 3 h), confirming that the strong LA Sn sites are more prone to hydration.[30] In this case, the pentacoordinated Sn is not detected in the hydrated redreox sample but in the dehydrated one. It seems that for the dehydrated redreox sample (dehydrated at 450 °C for 12 h under dynamic vacuum [10^{-2} mbar]), some Sn sites still interact with one H_2O-molecule. Consequently, it could be that these pentacoordinated Sn sites possess a very strong Lewis acidity and might be detected with CD_3CN-FTIR as strong LA Sn sites as well.

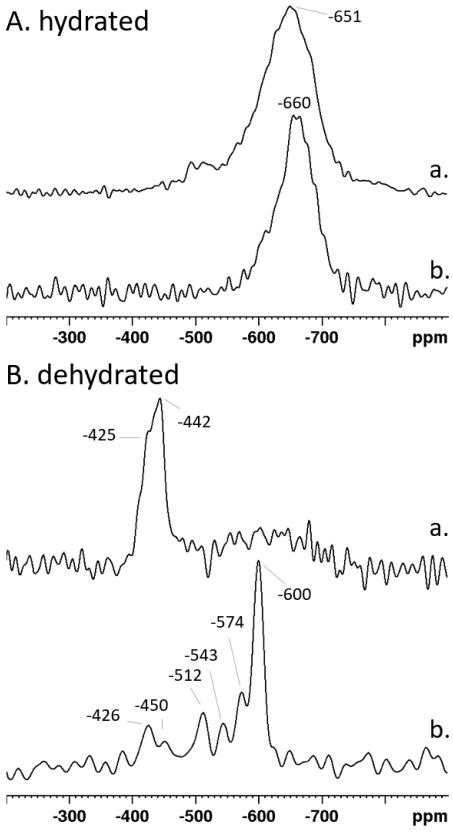


Figure 7. A. ^{119}Sn CP CPMG MAS NMR spectra of hydrated and **B.** ^{119}Sn DE CPMG MAS NMR spectra of dehydrated (a.) 10Snβ-N_2/air and (b.) 10Snβ-N_2/air-redreox catalysts.

We further evaluated if the SnO_2 species seen by solid-state ^{119}Sn NMR are also detected by PXRD. Figure 8 shows the diffraction patterns for Snβ-air, Snβ-N_2/air and SnO_2-deAlβ at varying Sn content with and without reduction-reoxidation. At 10 wt.% Sn, in all cases, sharper SnO_2 reflections (at 26.7, 33.9 and 52.3°) were indeed obtained after treatment. Interestingly, while for Snβ-air existing SnO_2 reflections sharpened after treatment, SnO_2 reflections appeared for Snβ-N_2/air-redreox as no crystalline SnO_2 particles were detected before treatment. Hence, PXRD data confirms that larger and more crystalline SnO_2 clusters are formed after treatment at high Sn loading (> 5 wt.%). For low Sn loadings (≤ 5 wt. %), however, no such SnO_2 reflections were apparent after treatment. Finally, for the untreated 5SnO_2 deAlβ sample, highly intense and sharp

SnO_2 signals are detected, which agree with the absence of LA density (FTIR). After reduction-reoxidation, the signals became less intense, which supports the improved incorporation of Sn(IV) into the framework.

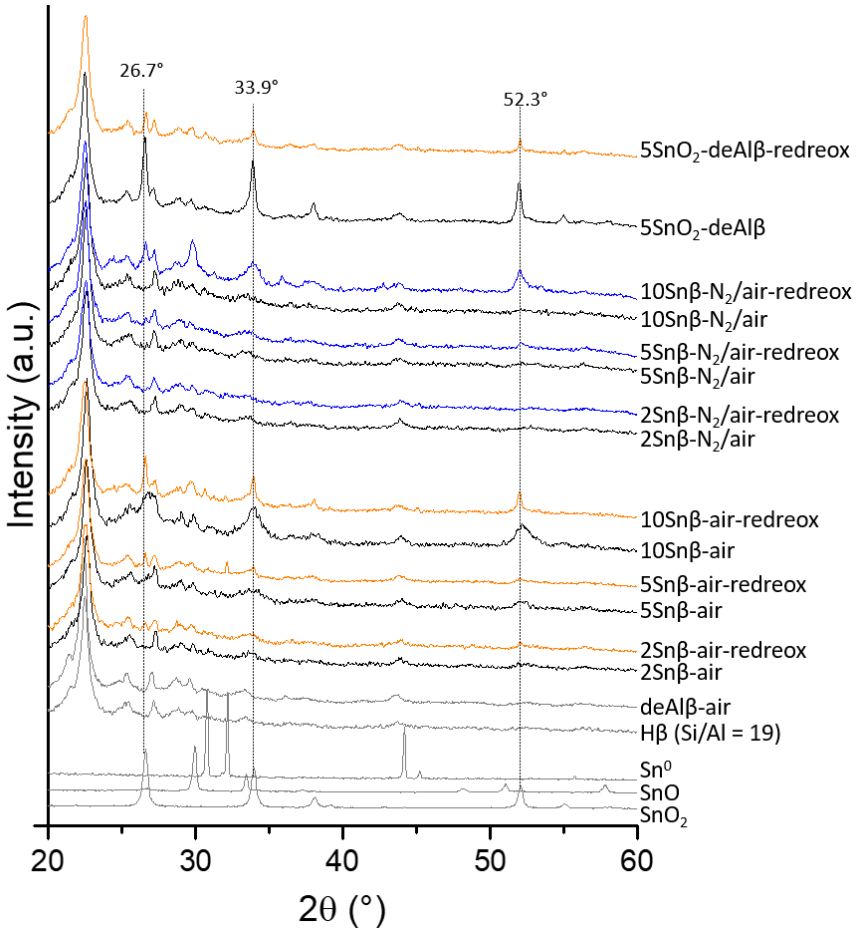


Figure 8. PXRD patterns of (un)treated Snβ-air, Snβ-N_2/air and SnO_2-deAlβ with varying Sn content and calcination method benchmarked against dealβ-air, parent Hβ (Si/Al=19) and pure Sn^0, SnO and SnO_2. redreox: reduced (in H_2) at 700 °C and reoxidized (in air) at 550 °C.

To evaluate how Sn dispersion inside the β zeolite is affected by the reduction step, surface (XPS) and bulk (ICP-AES) Sn/Si ratios are compared in Figure 9. The XPS spectra of the Snβ samples (Figure S9) display signals of Sn $3d_{3/2}$ and $3d_{5/2}$ with binding energies at 495.8 and 487.5 eV, respectively, which is indicative of Sn(IV).[70] At high Sn loadings (> 5 wt. %), the Sn to Si

ratio decreased drastically after the reduction-reoxidation cycle for both the air and N_2/air catalysts. This means a better infiltration of the Sn species into the β zeolite. This is in line with a recent paper observing an increased amount of Sn in the core region of a K-PtSn-MFI zeolite via STEM-EDS and HAADF after reduction at 650 °C.[71] These results confirm that mobile Sn(II)O and metallic Sn(0) species can migrate during the reduction step from the surface to the core of the β-zeolite. Hence, increasing Sn dispersion inside the β zeolite seems to align with a higher catalytic BVO and MPV activity. For the 5Snβ-N_2/air catalyst, no change in Sn dispersion into the crystal upon reduction was observed. Activity-wise this treated 5Snβ-N_2/air is very similar to the non-reduced sample, further confirming the importance of the Sn dispersion parameter for the catalytic activity.

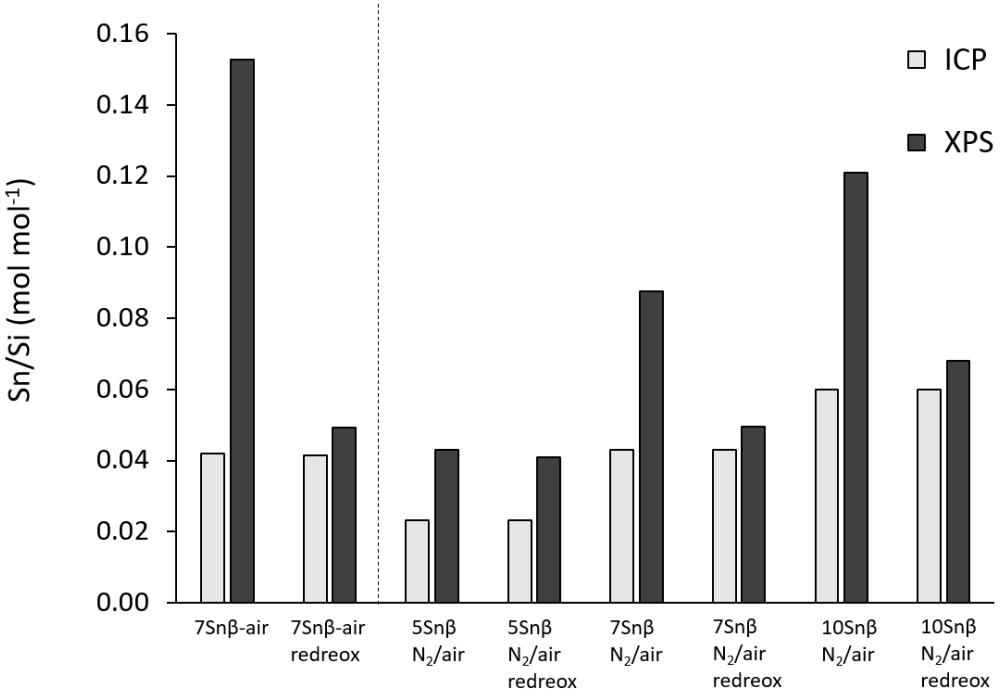


Figure 9. Bulk and surface Sn content (in Sn/Si) as measured by ICP (grey) and XPS (black) for selected Snβ XSnβ-Y-(redreox) with Sn content X (wt. %), heat treatment Y. redreox: reduced (in H_2) at 700 °C and reoxidized (in air) at 550 °C.

Finally, with ^{119}Sn Mössbauer spectroscopy we investigated if at high Sn loadings, we can detect the formation of SnO_2 clusters together with new LA Sn sites. The results of the non-treated and redreox catalysts are presented in Figure 10 and Table 1. The left and right end of the bar in Figure 10 represent the resulting IS and QS-values, respectively, of the Sn(IV) component in each sample. A high QS together with a negative IS value for Sn(IV), suggest a more distorted first neighbour environment, as discussed in section 1, and hence a better on-average incorporation of Sn into the framework.[8,51,67,72] For the air-calcined sample with low Sn loading, a significant decrease in IS (-0.08 *vs.* 0.02 $mm \cdot s^{-1}$) and an increase in QS (0.57 *vs.* 0.50 $mm \cdot s^{-1}$) after the redreox step confirms the better incorporation of Sn into the beta framework, which agrees with the increased Sn dispersion (Figure S7). For N_2/air-catalysts with ≤ 5 wt. % of Sn, the IS- and QS-values for the reduced and non-reduced catalysts are very similar. As already discussed in section 1, Sn is already well dispersed after the pre-pyrolysis step (Sn dispersion up to 60%), and thus no major improvement was seen after the redreox step. Finally, for high Sn loading (10 wt. %), a significant decrease in QS is obtained for the N_2/air sample after the redox step (0.75 to 0.53 $mm \cdot s^{-1}$). Since SnO_2 has an IS and QS of 0.04 and 0.50 $mm \cdot s^{-1}$ (Table 1, entry 23), the lower QS is in line with the presence of more SnO_2 clusters. In contrast, the IS-value for this sample is retained at a similar level, even becoming slightly more negative (-0.08 *vs*. -0.06). This result could justify the presence of pentacoordinated Sn sites, detected via NMR, which seem to shift the average IS of the Sn(IV) component towards a slightly more negative IS-value.

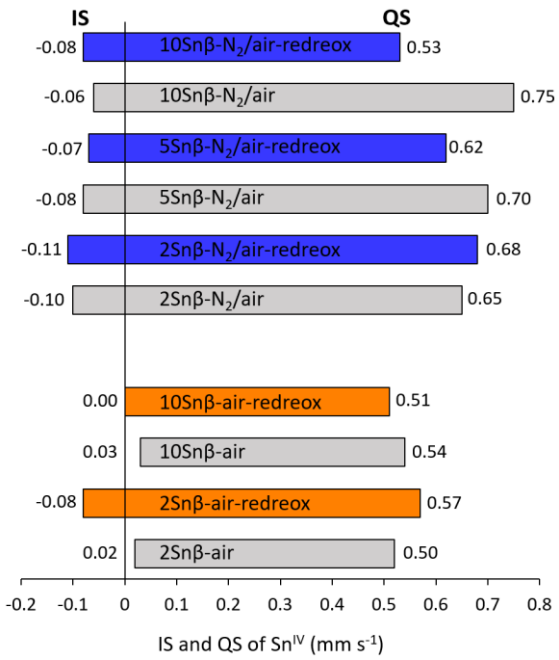


Figure 10. Comparative figure of the isomer shift (IS) and quadrupole splitting (QS) of the Sn(IV) species in Snβ-(redreox) catalysts. The left and right end of the bar represent the IS and QS-value, respectively.

DISCUSSION AND CONCLUSION

In this work, it is shown that for low Sn loadings (up to 5 wt. %), inactive SnO_2 clusters (≤ 5 nm) can be redispersed via a tandem reduction-reoxidation. SnO_2 clusters are reduced towards mobile Sn(II)O species which will interact with the zeolite. Further reduction towards metallic Sn appeared as well, but at low Sn loading these metallic particles are not likely to aggregate in large metal particles. After reoxidation, higher LA density and BVO activity are obtained as more framework Sn or small SnO_2 clusters are created. The redispersion hypothesis for low Sn loadings was further corroborated by using SnO_2 as a Sn precursor. The SnO_2-deAlβ catalyst, having no LA density and no catalytic activity, could be activated by an intermediate reduction step, resulting in a higher Sn dispersion and a decent catalytic BVO activity by the formation of framework Sn and

small SnO_2-clusters (FTIR, PXRD). For Snβ catalysts of low loadings with a high Sn dispersion (N_2/air catalysts), no improvement in LA density and activity was observed after the redreox step. This demonstrated that already well incorporated Sn species (framework or small SnO_2 clusters in pores) are not negatively affected by this treatment.

At high Sn loadings (> 5wt. %), however, a deviation in catalytic BVO activity and LA density appeared. For all catalysts with a Sn content > 5 wt. % (air and N_2/air), after the redreox step, a plateau was reached for the LA density, but simultaneously the BVO activity kept increasing (up to 140 $mM_{CL} \cdot h^{-1}$, Figure 4B). More specifically, the total LA density of 10Snβ-N_2/air relatively decreased by 30% after the redreox step, while in contrast the BVO activity increased by 50%. This 10Snβ-N_2/air-redreox catalysts was not only more active in the BVO reaction, but also in the MPV reaction. For both reactions, similar E_a-values (and thus enthalpic levels) were obtained after the redreox step, but the pre-exponential factors (k_0) were multiplied by a factor 2. As previously mentioned, the k_0-factor is influenced by (i) the number of active sites and (ii) entropic change of the transition state. Since the amount of LA sites (as calculated by Py and CD_3CN-FTIR) was lower for the redreox catalyst, the higher rate of the treated catalysts in the MPV and BVO reactions could predominantly be ascribed to entropic effects. This suggests that the active sites of the redreox catalysts form the required substrate orientation better, decreasing the loss of entropy upon forming the transition state.

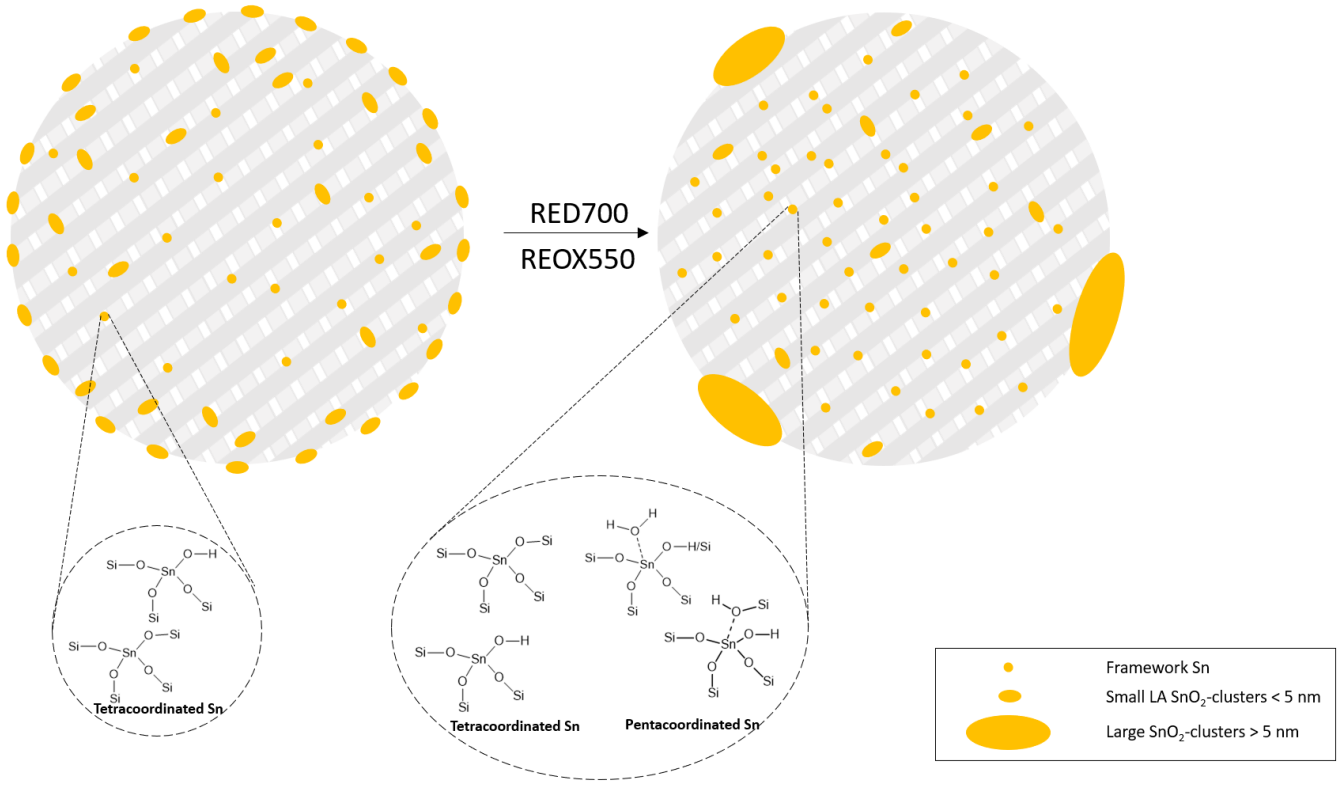
Hence, to shed light on the type of active Sn species and its distribution, the differences and similarities of the 10Snβ-N_2/air catalyst and its redreox variant are summarized below. Both catalysts showed a similar Sn content (ICP) and pore volume (N_2 physisorption, Table S2). 10Snβ-N_2/air-redreox possessed similar number of strong LA Sn sites, but the weak LA Sn sites drastically decreased compared to the non-treated catalyst (CD_3CN-FTIR, Figure 5 B and C).

Major differences were detected via ^{119}Sn SS NMR (Figure 7). The dehydrated redreox catalyst contained less framework sites (both strong and weak Sn sites at -426 and -450 ppm, respectively). Instead, a SnO_2 signal arose at -600 ppm, and signals appeared between -510 to -575 ppm, which are suggested to be pentacoordinated Sn species. The SnO_2 clusters of the redreox catalysts were visible with XRD, whereas no SnO_2 signals appeared for the non-reduced catalysts (Figure 8). Interestingly, by comparing the surface and bulk Sn/Si ratios (XPS and ICP, Figure 9) the Sn species were better dispersed in the β zeolite after the redreox step. Finally, ^{119}Sn Mössbauer spectroscopy (Table 1, Figure 10) showed a slightly more negative IS (-0.08 *vs.* -0.06 $mm \cdot s^{-1}$), together with a lower QS (0.53 *vs.* 0.75 $mm \cdot s^{-1}$) for the redreox catalyst which could indicate the presence of pentacoordinated Sn sites.

In scheme 2 a possible redreox process is displayed at high Sn loading. Although no SnO_2 clusters are detected via XRD (SnO_2 < 5 nm) for 10Snβ-N_2/air, XPS/ICP results showed that the zeolite possessed a significant amount of Sn-(clusters) at the surface of the β-zeolite, in addition to framework Sn and small SnO_2 clusters inside the pores. Upon reduction, surface Sn(IV)O_2 species are reduced towards mobile Sn(II)O species which can (i) diffuse inside the zeolite and interact with silanol nests or (ii) encounter and collide with other Sn-particles at the surface, creating large clusters. The theoretical maximum incorporation of framework Sn inside a β zeolite (starting with a parent zeolite with Si/Al ratio of 19) is 9.2 wt % provided that all silanol nests, created by removal of Al, are used as Sn anchoring points. At high reduction temperatures, a part of the silanol nests will condense to siloxane bridges, which diminishes the framework Sn anchoring points. Hence, as there are only a limited number of Sn anchoring points in the zeolite framework, the agglomeration of Sn species to form SnO_2 clusters (after reoxidation) will happen more frequently at high Sn loading. Moreover, a reduced Snβ with a high Sn content contains a

higher absolute amount of metallic Sn. Since it has been reported that, in general, larger metal particle sizes and/or higher metal contents complicate the redispersion process,[73–75] the formation of large metallic clusters (as detected with XRD) could explain the lower final Sn dispersion.

Since the total amount of Sn (in mol) on the crystal surface is less after reduction, it means that more Sn is incorporated inside the zeolite (as framework Sn or small SnO_2 clusters since large SnO_2 clusters are too big to diffuse inside the pores). The lower LA density after the treatment could be explained by the fact that small SnO_2 clusters on the surface of the untreated zeolite possess Lewis acidity. However, they are not very active in the reaction because pore-confinement is essential to allow the adequate substrate conformation. After the treatment, the larger particles created at the surface (due to Sn collision and clustering) are not Lewis acidic (which agrees with the lower total Lewis acidity), but more active LA Sn sites are created inside the pores which could explain the increased pre-exponential factor (per LA site measured). It could be that the pentacoordinated Sn species detected by NMR, are very strong LA Sn sites which have the adequate orientation and hence, are more efficient in the BVO and MPV reaction. Future work will further study the pentacoordinated Sn species in greater detail, with the aim of identifying their local environment and interactions with the substrates. Moreover, since it is known that large metal particle sizes and high metal contents hamper the redispersion of the metal oxides,[73–75] ongoing work focuses on applying milder reduction conditions (such as using CO instead of H_2 as reducing agent) to prevent undesired metal formation, and to produce outstanding Snβ catalysts.



Scheme 2. Illustration of the proposed changes of the Sn species in a β zeolite at high Sn loading during the tandem reduction-reoxidation and the tentative configurations of the tetracoordinated and pentacoordinated Sn Lewis acid sites.

MATERIAL AND METHODS

Catalyst synthesis

synthesis

A calcined commercial Al-β (CP814c, Zeolyst International, SiO_2/Al_2O_3 = 38) was dealuminated by stirring the zeolite powder for 20 h in a 65% nitric acid solution (20 $mL \cdot g^{-1}$ of zeolite) at 100 °C. Afterwards, the solids were filtered and washed thoroughly with water and dried overnight at 60 °C. To remove any physisorbed water the dealuminated β was stored in an oven at 150 °C. The procedure of Hammond was followed for the solid state synthesis.[44,45] The appropriate amount of Sn precursor (Sn(II) acetate or SnO_2 with particle size < 100 nm) was added to the

dealuminated β and manually ground for 10 min in a pestle and mortar. Two calcination procedure were used. In this first method (abbreviated as air), the sample was heated under static air in a muffle furnace to 550 °C (2 °C·min^{-1}) for 6 h. In the second method (abbreviated as N_2/air), the sample was heated in a quartz tube inside a tubular oven to 550 °C (2 °C·min^{-1}) first in a N_2-flow (3 h) and subsequently in an air-flow (3 h). Gas flow rates of 20mL·min^{-1} were employed. The procedure of Gounder *et al.* was followed for the grafting method.[43] The dried dealuminated β was added to dichloromethane (DCM) solvent (dried for 3 days under Ar using molecular 3A sieves) in a round-bottom flask and the appropriate amount of $SnCl_4$ (1 M in DCM) was added via a syringe. The solution was heated for 7 h at 50 °C under reflux conditions with N_2. Afterwards the zeolite was rinsed with methanol and dried overnight at 60 °C. The recovered solids were calcined for 6 h at 200 °C (3 °C·min^{-1}) and 6 h at 550 °C (3 °C·min^{-1}).

Reduction and reoxidation of Snβ

Reduction of the calcined samples was performed in a quartz U-tube with a quartz window for DRUV-vis measurements. The U-tube was placed in tubular oven and heated (5 °C·min^{-1}) to the desired temperature under a flow of H_2 for 2 h. If the sample was reoxidized, the same set-up was used and the reduced catalyst was heated (5 °C·min^{-1}) in an air-flow to the desired reoxidation temperature for 2 h.

Characterization techniques

TPR-MS analysis was performed in a horizontal home-made oven with temperature control, coupled to a Pfeiffer Omnistar Mass spectrometer. The catalyst powder was pelletized (sieve fraction 250-500 μm) and 200 mg was placed inside a quartz tube. The sample was pretreated at 400 °C in He for 2 hours and was cooled to 100 °C before starting the measurement. Next, the sample was heated at 10 °C·min^{-1} in 14.8 ml·min^{-1} of a 5% H_2 in He-flow to 1000 °C. M/e of 2

(H_2) and 18(H_2O) were tracked with the MS. **DRUV-vis** measurements were performed in quartz U-tubes equipped with a quartz window. The samples were pretreated (reduced or reoxidized) inside the U-tubes and measured, after cooling, on an Agilent Cary 5000 spectrophotometer. Dried barium sulfate was used as the diffuse reflectance standard. **PXRD** patterns were recorded on a high-throughput STOE Stadi P Combi diffractometer in the transmission mode equipped with Cu-Kα_1 source and IP-PSD detector. **N_2 sorption** measurements were performed using a Micromeritics Instruments Tristar 3000 at 77 K. Samples were degassed under N_2-flow at 300 °C for 6 h prior to measurement. The relative nitrogen pressure was varied between 0.01 and 0.99 (p/p_0). Pore volumes were calculated by the t-plot method. **Elemental analysis** was performed using an ICP-AES (Perkin Elmer Optima 3300 DV) with signals for Sn, Al, and Si at 189.9, 238.2, and 251.6 nm, respectively. Before ICP-AES, the samples were decomposed with lithium metaborate at 1000 °C and dissolved in 5% HCl in Milli-Q water. **FTIR** measurements were performed on a Nicolet 6700 Spectrometer equipped with DTGS detector. Samples were pressed into self-supporting wafers (with a rectangular shape with size around 1.6 cm x 1.1 cm) and degassed at 400 °C *in vacuo* for 1 h before measurements. LA sites were analyzed with gas-phase pyridine or deuterated acetonitrile. For pyridine adsorption, the samples were subjected to a flow of pyridine (20 - 25 mbar) until saturation at 50 °C. Spectra were recorded at 150 °C *in vacuo* after equilibration for 40 min. 1.42 $cm \cdot \mu mol^{-1}$ was used as integrated molar extinction coefficient for calculations of LA density at 1451 cm^{-1}.[63] Deuterated acetonitrile (CD3CN) was adsorbed at 30 °C. The samples were exposed to sequential doses of 4 mbar of probe molecule until saturation, which was evidenced when gas-phase CD_3CN (2267 cm^{-1}) appeared. Once saturated, a spectrum was recorded at 30 °C after 30 s *in vacuo*. The spectra were deconvoluted in open Sn sites (2316 cm^{-1}), closed Sn sites (2308 cm^{-1}), SnO_2 (2287 cm^{-1}), silanol groups (2275 cm^{-1}), and physisorbed

or gas-phase CD_3CN (2265 cm^{-1}) with OMNIC software. All peaks were fitted using mixed Gaussian-Lorentzian peaks (50/50) except for the peak corresponding to physisorbed CD_3CN, which was fitted using a fully Lorentzian (0/100) peak. For all deconvolutions, a peak centers variation of ± 3 cm^{-1} was allowed and FWHM values ranged from 5- 20 cm^{-1}.[3] For strong and weak Sn sites, integrated molar extinction coefficient of 1.04 and 2.04, respectively, were used.[63] For all probe molecules, spectra of unloaded materials were recorded at the same temperature as the reference spectra. The number of LA sites titrated by the probe molecules was calculated using the following equation.

$$\text{LA density } (\mu mol \cdot g^{-1}) = \frac{\text{integrated peak area } (cm^{-1})}{\text{molar extinction coefficient } (cm\ \mu mol^{-1})} \times \frac{A_{wafer}\ (cm^2)}{m\ (g)} \quad (1)$$

With A_{wafer} and m the area and the mass of the dry wafer, respectively.

Sn dispersion is calculated by assuming 1 active Sn site per adsorbed molecule of pyridine divided by the total amount of Sn present (calculated via ICP-AES).

XPS measurements were carried out on a SSX 100/206 photoelectron spectrometer from Surface Science Instruments (USA), equipped with a monochromatized Al-Kα radiation (1486 eV). The sample powders, pressed in small stainless troughs of 4 mm diameter, were placed on an insulating home-made ceramic carousel. The pressure in the analysis chamber was around 10^{-6} Pa. The analyzed area was ~1.4 mm^2 and the pass energy was set at 150 eV. The Si2p peak of silicon was fixed to 103.5 eV to set the binding energy scale. Data treatment was performed with the CasaXPS program (Casa Software Ltd, UK); spectra were decomposed with the least squares fitting routine provided by the software with a Gaussian/Lorentzian (85/15) product function, after the baseline was subtracted. **^{119}Sn Mössbauer spectra** of the powder samples were collected at 77 K in transmission geometry, using a constant-acceleration Mössbauer spectrometer equipped with a $Ca^{119m}SnO_3$ source kept at RT and a variable-temperature (Thor Cryogenics) liquid nitrogen bath

cryostat. The spectrometer was calibrated with metallic iron at room temperature and 77 K. Analyses of the spectra were performed by the IMSG code using Lorentzian-type lines.[76] To prevent re-oxidation, the reduced samples were stored, sealed and transported in N_2-atmosphere and the corresponding Mössbauer sample holder was prepared and sealed in a glovebox under N_2-atmosphere prior to its measurement. The non-reduced or reoxidized samples were transported after drying at 550 °C (or as specified) in air in a sealed vial. The corresponding Mössbauer sample holder was rapidly prepared and sealed in ambient conditions prior to its measurements. **^{119}Sn MAS NMR** direct excitation combined with CPMG echo-train acquisition (DE-CPMG) and cross-polarization combined with CPMG echo-train acquisition (CP-CPMG) measurements were carried out following the method described by Ivanova.[64] Measurements were carried out using a Bruker Avance III HD spectrometer operating at 149.15 MHz for ^{119}Sn and a 4 mm (rotor outside diameter) magic-angle spinning probe. Direct excitation measurements were carried out using a 60 s recycle delay. Cross polarisation measurements were carried out with a 1 s recycle delay and 3 ms contact time. A spin rate of 10 kHz was used for all measurements. Spectral referencing is with respect to $Sn(CH_3)_4$ carried out by setting the resonance from an external sample of $Sn(C_6H_{11})_4$ to -97.4 ppm. Other experimental details are given in Table S3. Where accumulation times exceed 24 hours, the results from multiple identical measurements were added together. Spectra for hydrated samples were first recorded on samples that had been stored under ambient conditions. Dehydrated samples were subsequently formed through dehydration at 450 °C (ramp rate = 5 °C·min) under dynamic vacuum (below 10^{-2} mbar, attached to a Schlenk line) in a quartz tube for 12 h. The quartz tube was subsequently transferred to an argon filled glovebox, where samples were transferred to a 4 mm rotor. Approximately 60 - 80 mg of solid was loaded into the rotor.

Catalytic reactions

BVO and MPV reactions were performed in magnetically stirred thick-walled glass reactors, capped with a rubber stopper and placed in a temperature-controlled copper block. The BVO reaction was conducted at 80 °C (or as mentioned), 10 mg of catalyst was added to 330 mM of cyclohexanone in 5 mL of 1,4-dioxane. The glass reactor was heated to the required temperature for 10 min, prior to the addition of 50 wt. % H_2O_2 in an H_2O_2/ketone ratio of 1.5. The MPV reaction was conducted at 80 °C (or as mentioned), 15 mg of catalysts was added to a 7 mL solution of 0.2 M of CHO in 2-butanol. For both reactions, biphenyl was used as internal standard for chromatographic analysis. To determine the initial formation rate, samples were taken at regular time intervals and filtered to remove the catalysts. Each r_0 was determined from the initial linear part of the kinetic plot. For the BVO reactions, samples used for the calculation of the initial formation rate contained a CL-yield below 10%. MnO_2 powder was added to the aliquots to decompose H_2O_2, which is still present in a large amount and is detrimental for the GC-column. After decomposition of H_2O_2 to O_2 and H_2O, MnO_2 powder was removed by filtration. The aliquots of the BVO and MPV reaction were quantitatively analyzed on a Hewlett Packard HP 6890 GC equipped with an HP 7683 autosampler, a 30m CP-wax-52 CB column and an FID detector. Identification of products was based on retention time analysis. Apparent activation energy (E_a), pre-exponential factor (k_0) for the reactions were calculated via following equations:

Arrhenius equation: $\ln k = \ln k_0 - \frac{E_a}{R} \cdot \frac{1}{T}$ (2)

Where R is the gas constant.

ASSOCIATED CONTENT

Supporting information

TPR-MS and ^{119}Sn Mössbauer spectra, PXRD data of reduced Snβ materials, kinetic and Arrhenius plots for the BVO and MPV reactions, Sn dispersion against Sn content, illustrative CD_3CN-FTIR and XPS spectra, general overview of the main catalysts samples and the applied reactions and characterization techniques, physicochemical properties of the Snβ samples and the main acquisition parameters of the ^{119}Sn CP and DE CPMG MAS NMR spectra.

AUTHOR INFORMATION

Corresponding Authors

*E-mail: michiel.dusselier@kuleuven.be

*E-mail: bert.sels@kuleuven.be

Notes

The authors declare no competing financial interest

ACKNOWLEDGMENTS

EP thanks FWO for the SB PhD fellowship (grant 1S96020N). IK acknowledges FWO (grant 1260321N) for financial support. DPD thanks the Francqui Foundation for his Francqui Research Professor chair. RT thanks the Durham University Solid State NMR service for NMR data acquisition and helpful discussions.

REFERENCES

(1) Corma, A.; Domine, M. E.; Nemeth, L.; Valencia, S. Al-Free Sn-Beta Zeolite as a Catalyst for the Selective Reduction of Carbonyl Compounds (Meerwein−Ponndorf−Verley Reaction). *J. Am. Chem. Soc.* **2002**, *124* (13), 3194–3195. https://doi.org/10.1021/ja012297m.

(2) Dijkmans, J.; Schutyser, W.; Dusselier, M.; Sels, B. F. Snβ-Zeolite Catalyzed Oxido-Reduction Cascade Chemistry with Biomass-Derived Molecules. *Chem. Commun.* **2016**, *52* (40), 6712–6715. https://doi.org/10.1039/C6CC00199H.

(3) Di Iorio, J. R.; Johnson, B. A.; Román-Leshkov, Y. Ordered Hydrogen-Bonded Alcohol Networks Confined in Lewis Acid Zeolites Accelerate Transfer Hydrogenation Turnover Rates. *J. Am. Chem. Soc.* **2020**, *142* (45), 19379–19392. https://doi.org/10.1021/jacs.0c09825.

(4) Corma, A.; Nemeth, L. T.; Renz, M.; Valencia, S. Sn-Zeolite Beta as a Heterogeneous Chemoselective Catalyst for Baeyer–Villiger Oxidations. *Nature* **2001**, *412*, 423.

(5) Yakabi, K.; Milne, K.; Buchard, A.; Hammond, C. Selectivity and Lifetime Effects in Zeolite-Catalysed Baeyer–Villiger Oxidation Investigated in Batch and Continuous Flow. *ChemCatChem* **2016**, *8* (22), 3490–3498. https://doi.org/10.1002/cctc.201600955.

(6) Yakabi, K.; Mathieux, T.; Milne, K.; López-Vidal, E. M.; Buchard, A.; Hammond, C. Continuous Production of Biorenewable, Polymer-Grade Lactone Monomers through Sn-β-Catalyzed Baeyer-Villiger Oxidation with H 2 O 2. *ChemSusChem* **2017**, *10* (18), 3652–3659. https://doi.org/10.1002/cssc.201701298.

(7) Schutyser, W.; den Bosch, S.; Dijkmans, J.; Turner, S.; Meledina, M.; Van Tendeloo, G.; Debecker, D. P.; Sels, B. F. Selective Nickel-Catalyzed Conversion of Model and Lignin-Derived Phenolic Compounds to Cyclohexanone-Based Polymer Building Blocks. *ChemSusChem* **2015**, *8* (10), 1805–1818. https://doi.org/10.1002/cssc.201403375.

(8) Peeters, E.; Pomalaza, G.; Khalil, I.; Detaille, A.; Debecker, D. P.; Douvalis, A. P.; Dusselier, M.; Sels, B. F. Highly Dispersed Sn-Beta Zeolites as Active Catalysts for Baeyer–Villiger Oxidation: The Role of Mobile, In Situ Sn(II)O Species in Solid-State Stannation. *ACS Catal.* **2021**, *11* (10), 5984–5998. https://doi.org/10.1021/acscatal.1c00435.

(9) Moliner, M.; Román-Leshkov, Y.; Davis, M. E. Tin-Containing Zeolites Are Highly Active Catalysts for the Isomerization of Glucose in Water. *Proc. Natl. Acad. Sci. U. S. A.* **2010**, *107* (14), 6164–6168. https://doi.org/10.1073/pnas.1002358107.

(10) Román-Leshkov, Y.; Moliner, M.; Labinger, J. A.; Davis, M. E. Mechanism of Glucose Isomerization Using a Solid Lewis Acid Catalyst in Water. *Angew. Chemie Int. Ed.* **2010**, *49* (47), 8954–8957. https://doi.org/10.1002/anie.201004689.

(11) Choudhary, V.; Pinar, A. B.; Sandler, S. I.; Vlachos, D. G.; Lobo, R. F. Xylose Isomerization to Xylulose and Its Dehydration to Furfural in Aqueous Media. *ACS Catal.* **2011**, *1* (12), 1724–1728. https://doi.org/10.1021/cs200461t.

(12) Gunther, W. R.; Wang, Y.; Ji, Y.; Michaelis, V. K.; Hunt, S. T.; Griffin, R. G.; Román-Leshkov, Y. Sn-Beta Zeolites with Borate Salts Catalyse the Epimerization of Carbohydrates via an Intramolecular Carbon Shift. *Nat. Commun.* **2012**, *3* (1), 1109. https://doi.org/10.1038/ncomms2122.

(13) Lew, C. M.; Rajabbeigi, N.; Tsapatsis, M. Tin-Containing Zeolite for the Isomerization of Cellulosic Sugars. *Microporous Mesoporous Mater.* **2012**, *153*, 55–58. https://doi.org/https://doi.org/10.1016/j.micromeso.2011.12.020.

(14) Dijkmans, J.; Gabriels, D.; Dusselier, M.; de Clippel, F.; Vanelderen, P.; Houthoofd, K.; Malfliet, A.; Pontikes, Y.; Sels, B. F. Productive Sugar Isomerization with Highly Active Sn in Dealuminated Beta Zeolites. *Green Chem.* **2013**, *15* (10), 2777–2785. https://doi.org/10.1039/C3GC41239C.

(15) Bermejo-Deval, R.; Orazov, M.; Gounder, R.; Hwang, S.-J.; Davis, M. E. Active Sites in Sn-Beta for Glucose Isomerization to Fructose and Epimerization to Mannose. *ACS Catal.* **2014**, *4* (7), 2288–2297. https://doi.org/10.1021/cs500466j.

(16) Padovan, D.; Botti, L.; Hammond, C. Active Site Hydration Governs the Stability of Sn-Beta during Continuous Glucose Conversion. *ACS Catal.* **2018**, *8* (8), 7131–7140. https://doi.org/10.1021/acscatal.8b01759.

(17) Botti, L.; Navar, R.; Tolborg, S.; Martinez-Espin, J. S.; Padovan, D.; Taarning, E.; Hammond, C. Influence of Composition and Preparation Method on the Continuous Performance of Sn-Beta for Glucose-Fructose Isomerisation. *Top. Catal.* **2019**, *62* (17), 1178–1191. https://doi.org/10.1007/s11244-018-1078-z.

(18) Botti, L.; Meier, S.; Hammond, C. Mechanistic Studies of Continuous Glucose Upgrading over Lewis Acidic Silicates by Operando UV–Vis and HSQC NMR. *ACS Catal.* **2021**, *11* (3), 1296–1308. https://doi.org/10.1021/acscatal.0c03638.

(19) Holm, M. S.; Saravanamurugan, S.; Taarning, E. Conversion of Sugars to Lactic Acid Derivatives Using Heterogeneous Zeotype Catalysts. *Science (80-.).* **2010**, *328* (5978), 602–605. https://doi.org/10.1126/science.1183990.

(20) Orazov, M.; Davis, M. E. Tandem Catalysis for the Production of Alkyl Lactates from Ketohexoses at Moderate Temperatures. *Proc. Natl. Acad. Sci.* **2015**, *112* (38), 11777–11782. https://doi.org/10.1073/pnas.1516466112.

(21) Tang, B.; Li, S.; Song, W.-C.; Yang, E.-C.; Zhao, X.-J.; Guan, N.; Li, L. Fabrication of Hierarchical Sn-Beta Zeolite as Efficient Catalyst for Conversion of Cellulosic Sugar to Methyl Lactate. *ACS Sustain. Chem. Eng.* **2020**, *8* (9), 3796–3808. https://doi.org/10.1021/acssuschemeng.9b07061.

(22) Van de Vyver, S.; Odermatt, C.; Romero, K.; Prasomsri, T.; Román-Leshkov, Y. Solid Lewis Acids Catalyze the Carbon–Carbon Coupling between Carbohydrates and Formaldehyde. *ACS Catal.* **2015**, *5* (2), 972–977. https://doi.org/10.1021/cs5015964.

(23) Lewis, J. D.; de Vyver, S.; Román-Leshkov, Y. Acid–Base Pairs in Lewis Acidic Zeolites Promote Direct Aldol Reactions by Soft Enolization. *Angew. Chemie Int. Ed.* **2015**, *54* (34), 9835–9838. https://doi.org/10.1002/anie.201502939.

(24) Boronat, M.; Concepción, P.; Corma, A.; Renz, M.; Valencia, S. Determination of the Catalytically Active Oxidation Lewis Acid Sites in Sn-Beta Zeolites, and Their Optimisation by the Combination of Theoretical and Experimental Studies. *J. Catal.* **2005**, *234* (1), 111–118. https://doi.org/https://doi.org/10.1016/j.jcat.2005.05.023.

(25) Bermejo-Deval, R.; Assary, R. S.; Nikolla, E.; Moliner, M.; Román-Leshkov, Y.; Hwang,

S.-J.; Palsdottir, A.; Silverman, D.; Lobo, R. F.; Curtiss, L. A.; Davis, M. E. Metalloenzyme-like Catalyzed Isomerizations of Sugars by Lewis Acid Zeolites. *Proc. Natl. Acad. Sci.* **2012**, *109* (25), 9727–9732. https://doi.org/10.1073/pnas.1206708109.

(26) Bellussi, G.; Carati, A.; Clerici, M. G.; Maddinelli, G.; Millini, R. Reactions of Titanium Silicalite with Protic Molecules and Hydrogen Peroxide. *J. Catal.* **1992**, *133* (1), 220–230. https://doi.org/https://doi.org/10.1016/0021-9517(92)90199-R.

(27) Notari, B. Titanium Silicalites. *Catal. Today* **1993**, *18* (2), 163–172. https://doi.org/https://doi.org/10.1016/0920-5861(93)85029-Y.

(28) Gordon, C. P.; Engler, H.; Tragl, A. S.; Plodinec, M.; Lunkenbein, T.; Berkessel, A.; Teles, J. H.; Parvulescu, A.-N.; Copéret, C. Efficient Epoxidation over Dinuclear Sites in Titanium Silicalite-1. *Nature* **2020**, *586* (7831), 708–713. https://doi.org/10.1038/s41586-020-2826-3.

(29) Weckhuysen, B. M. Fresh Evidence Challenges the Consensus View of Active Sites in an Industrial Catalyst. *Nature* **2020**, *586*, 678–679.

(30) Yakimov, A. V; Kolyagin, Y. G.; Tolborg, S.; Vennestrøm, P. N. R.; Ivanova, I. I. 119Sn MAS NMR Study of the Interaction of Probe Molecules with Sn-BEA: The Origin of Penta- and Hexacoordinated Tin Formation. *J. Phys. Chem. C* **2016**, *120* (49), 28083–28092. https://doi.org/10.1021/acs.jpcc.6b09999.

(31) Hwang, S.-J.; Gounder, R.; Bhawe, Y.; Orazov, M.; Bermejo-Deval, R.; Davis, M. E. Solid State NMR Characterization of Sn-Beta Zeolites That Catalyze Glucose Isomerization and Epimerization. *Top. Catal.* **2015**, *58* (7), 435–440. https://doi.org/10.1007/s11244-015-0388-7.

(32) Boronat, M.; Corma, A.; Renz, M.; Sastre, G.; Viruela, P. M. A Multisite Molecular Mechanism for Baeyer–Villiger Oxidations on Solid Catalysts Using Environmentally Friendly H2O2 as Oxidant. *Chem. – A Eur. J.* **2005**, *11* (23), 6905–6915. https://doi.org/10.1002/chem.200500184.

(33) Boronat, M.; Corma, A.; Renz, M. Mechanism of the Meerwein−Ponndorf−Verley−Oppenauer (MPVO) Redox Equilibrium on Sn− and Zr−Beta Zeolite Catalysts. *J. Phys. Chem. B* **2006**, *110* (42), 21168–21174. https://doi.org/10.1021/jp063249x.

(34) Lewis, J. D.; de Vyver, S.; Crisci, A. J.; Gunther, W. R.; Michaelis, V. K.; Griffin, R. G.; Román-Leshkov, Y. A Continuous Flow Strategy for the Coupled Transfer Hydrogenation and Etherification of 5-(Hydroxymethyl)Furfural Using Lewis Acid Zeolites. *ChemSusChem* **2014**, *7* (8), 2255–2265. https://doi.org/10.1002/cssc.201402100.

(35) Bermejo-Deval, R.; Gounder, R.; Davis, M. E. Framework and Extraframework Tin Sites in Zeolite Beta React Glucose Differently. *ACS Catal.* **2012**, *2* (12), 2705–2713. https://doi.org/10.1021/cs300474x.

(36) Dai, W.; Lei, Q.; Wu, G.; Guan, N.; Hunger, M.; Li, L. Spectroscopic Signature of Lewis

Acidic Framework and Extraframework Sn Sites in Beta Zeolites. *ACS Catal.* **2020**, *10* (23), 14135–14146. https://doi.org/10.1021/acscatal.0c02356.

(37) Dai, W.; Lei, Q.; Wu, G.; Guan, N.; Hunger, M.; Li, L. Spectroscopic Signature of Lewis Acidic Framework and Extraframework Sn Sites in Beta Zeolites. *ACS Catal.* **2020**, *10* (23), 14135–14146. https://doi.org/10.1021/acscatal.0c02356.

(38) Tolborg, S.; Katerinopoulou, A.; Falcone, D. D.; Sádaba, I.; Osmundsen, C. M.; Davis, R. J.; Taarning, E.; Fristrup, P.; Holm, M. S. Incorporation of Tin Affects Crystallization, Morphology, and Crystal Composition of Sn-Beta. *J. Mater. Chem. A* **2014**, *2* (47), 20252–20262. https://doi.org/10.1039/C4TA05119J.

(39) Chang, C.-C.; Cho, H. J.; Wang, Z.; Wang, X.; Fan, W. Fluoride-Free Synthesis of a Sn-BEA Catalyst by Dry Gel Conversion. *Green Chem.* **2015**, *17* (5), 2943–2951. https://doi.org/10.1039/C4GC02457E.

(40) Li, P.; Liu, G.; Wu, H.; Liu, Y.; Jiang, J.; Wu, P. Postsynthesis and Selective Oxidation Properties of Nanosized Sn-Beta Zeolite. *J. Phys. Chem. C* **2011**, *115* (9), 3663–3670. https://doi.org/10.1021/jp1076966.

(41) Jin, J.; Ye, X.; Li, Y.; Wang, Y.; Li, L.; Gu, J.; Zhao, W.; Shi, J. Synthesis of Mesoporous Beta and Sn-Beta Zeolites and Their Catalytic Performances. *Dalt. Trans.* **2014**, *43* (22), 8196–8204. https://doi.org/10.1039/C4DT00567H.

(42) Dijkmans, J.; Demol, J.; Houthoofd, K.; Huang, S.; Pontikes, Y.; Sels, B. Post-Synthesis Snβ: An Exploration of Synthesis Parameters and Catalysis. *J. Catal.* **2015**, *330*, 545–557. https://doi.org/10.1016/j.jcat.2015.06.023.

(43) Vega-Vila, J. C.; Harris, J. W.; Gounder, R. Controlled Insertion of Tin Atoms into Zeolite Framework Vacancies and Consequences for Glucose Isomerization Catalysis. *J. Catal.* **2016**, *344*, 108–120. https://doi.org/https://doi.org/10.1016/j.jcat.2016.09.011.

(44) Hammond, C.; Conrad, S.; Hermans, I. Simple and Scalable Preparation of Highly Active Lewis Acidic Sn-β. *Angew. Chemie Int. Ed.* **2012**, *51* (47), 11736–11739. https://doi.org/10.1002/anie.201206193.

(45) Hammond, C.; Padovan, D.; Al-Nayili, A.; Wells, P. P.; Gibson, E. K.; Dimitratos, N. Identification of Active and Spectator Sn Sites in Sn-β Following Solid-State Stannation, and Consequences for Lewis Acid Catalysis. *ChemCatChem* **2015**, *7* (20), 3322–3331. https://doi.org/10.1002/cctc.201500545.

(46) Charvin, P.; Abanades, S.; Lemont, F.; Flamant, G. Experimental Study of SnO2/SnO/Sn Thermochemical Systems for Solar Production of Hydrogen. *AIChE J.* **2008**, *54* (10), 2759–2767. https://doi.org/https://doi.org/10.1002/aic.11584.

(47) Chen, X.-T.; Wang, K.-X.; Zhai, Y.-B.; Zhang, H.-J.; Wu, X.-Y.; Wei, X.; Chen, J.-S. A Facile One-Pot Reduction Method for the Preparation of a SnO/SnO2/GNS Composite for High Performance Lithium Ion Batteries. *Dalt. Trans.* **2014**, *43* (8), 3137–3143. https://doi.org/10.1039/C3DT52661E.

(48) Lázár, K.; Szeleczky, A. M.; Mal, N. K.; Ramaswamy, A. V. In Situ 119Sn-Mössbauer Spectroscopic Study on MR, MEL, and MTW Tin Silicalites. *Zeolites* **1997**, *19* (2), 123–127. https://doi.org/https://doi.org/10.1016/S0144-2449(97)00056-0.

(49) Chaudhari, K.; Das, T. K.; Rajmohanan, P. R.; Lazar, K.; Sivasanker, S.; Chandwadkar, A. J. Synthesis, Characterization, and Catalytic Properties of Mesoporous Tin-Containing Analogs of MCM-41. *J. Catal.* **1999**, *183* (2), 281–291. https://doi.org/https://doi.org/10.1006/jcat.1999.2394.

(50) Lázár, K.; Chandwadkar, A. J.; Fejes, P.; Čejka, J.; Ramaswamy, A. V. Valency Changes of Iron and Tin in Framework-Substituted Molecular Sieves Investigated by in Situ Mössbauer Spectroscopy. *J. Radioanal. Nucl. Chem.* **2000**, *246* (1), 143–148. https://doi.org/10.1023/A:1006718106583.

(51) Dijkmans, J.; Dusselier, M.; Janssens, W.; Trekels, M.; Vantomme, A.; Breynaert, E.; Kirschhock, C.; Sels, B. F. An Inner-/Outer-Sphere Stabilized Sn Active Site in β-Zeolite: Spectroscopic Evidence and Kinetic Consequences. *ACS Catal.* **2016**, *6* (1), 31–46. https://doi.org/10.1021/acscatal.5b01822.

(52) Sushkevich, V. L.; Ivanova, I. I.; Yakimov, A. V. Revisiting Acidity of SnBEA Catalysts by Combined Application of FTIR Spectroscopy of Different Probe Molecules. *J. Phys. Chem. C* **2017**, *121* (21), 11437–11447. https://doi.org/10.1021/acs.jpcc.7b02206.

(53) Schwenn, H.-J.; Wark, M.; Schulz-Ekloff, G.; Wiggers, H.; Simon, U. Electrical and Optical Properties of Zeolite y Supported Sno2 Nanoparticles. *Colloid Polym. Sci.* **1997**, *275* (1), 91–95. https://doi.org/10.1007/s003960050057.

(54) Ara, M. H. M.; Boroojerdian, P.; Javadi, Z.; Zahedi, S.; Morshadian, M. Nonlinear Optical Properties of Ultra-Fine Nanocrystalline SnO Synthesised through Microwave-Assisted Hydrothermal Route. *Micro Nano Lett.* **2011**, *6* (4), 249–252. https://doi.org/10.1049/mnl.2010.0219.

(55) Yan, Q.; Tao, S.; Toghiani, H. Optical Fiber Evanescent Wave Absorption Spectrometry of Nanocrystalline Tin Oxide Thin Films for Selective Hydrogen Sensing in High Temperature Gas Samples. *Talanta* **2009**, *77* (3), 953–961. https://doi.org/https://doi.org/10.1016/j.talanta.2008.07.066.

(56) Matsuo, H.; Katayama, M.; Minegishi, T.; Yamada, T.; Kudo, A.; Domen, K. Impact of Lattice Defects on Water Oxidation Properties in SnNb2O6 Photoanode Prepared by Pulsed-Laser Deposition Method. *J. Appl. Phys.* **2019**, *126* (9), 94901. https://doi.org/10.1063/1.5097731.

(57) Popescu, D. A.; Herrmann, J.-M.; Ensuque, A.; Bozon-Verduraz, F. Nanosized Tin Dioxide: Spectroscopic (UV–VIS{,} NIR{,} EPR) and Electrical Conductivity Studies. *Phys. Chem. Chem. Phys.* **2001**, *3* (12), 2522–2530. https://doi.org/10.1039/B100553G.

(58) Kozhukharov, V.; Vasilev, S. Mössbauer Spectroscopy Applied to Inorganic Materials. In *Characterization Techniques of Glasses and Ceramics*; Rincon, J. M., Romero, M., Eds.;

Springer Berlin Heidelberg: Berlin, Heidelberg, 1999; pp 199–219. https://doi.org/10.1007/978-3-662-03871-0_11.

(59) Dickson, D. P. E.; Berry, F. J. *Mössbauer Spectroscopy*; Cambridge University Press: Cambridge, 1986. https://doi.org/DOI: 10.1017/CBO9780511524233.

(60) Shamzhy, M.; Opanasenko, M.; Concepción, P.; Martínez, A. New Trends in Tailoring Active Sites in Zeolite-Based Catalysts. *Chem. Soc. Rev.* **2019**, *48* (4), 1095–1149. https://doi.org/10.1039/C8CS00887F.

(61) Qi, G.; Chu, Y.; Wang, Q.; Wang, X.; Li, Y.; Trébosc, J.; Lafon, O.; Xu, J.; Deng, F. Gem-Diol-Type Intermediate in the Activation of a Ketone on Sn-β Zeolite as Studied by Solid-State NMR Spectroscopy. *Angew. Chemie Int. Ed.* **2020**, *59* (44), 19532–19538. https://doi.org/10.1002/anie.202005589.

(62) Eyring, H. The Activated Complex in Chemical Reactions. *J. Chem. Phys.* **1935**, *3* (2), 107–115. https://doi.org/10.1063/1.1749604.

(63) Harris, J. W.; Cordon, M. J.; Iorio, J. R. Di; Vega-Vila, J. C.; Ribeiro, F. H.; Gounder, R. Titration and Quantification of Open and Closed Lewis Acid Sites in Sn-Beta Zeolites That Catalyze Glucose Isomerization. *J. Catal.* **2016**, *335*, 141–154. https://doi.org/10.1016/j.jcat.2015.12.024.

(64) Kolyagin, Y. G.; Yakimov, A. V; Tolborg, S.; Vennestrøm, P. N. R.; Ivanova, I. I. Application of 119Sn CPMG MAS NMR for Fast Characterization of Sn Sites in Zeolites with Natural 119Sn Isotope Abundance. *J. Phys. Chem. Lett.* **2016**, *7* (7), 1249–1253. https://doi.org/10.1021/acs.jpclett.6b00249.

(65) Kolyagin, Y. G.; Yakimov, A. V; Tolborg, S.; Vennestrøm, P. N. R.; Ivanova, I. I. Direct Observation of Tin in Different T-Sites of Sn-BEA by One- and Two-Dimensional 119Sn MAS NMR Spectroscopy. *J. Phys. Chem. Lett.* **2018**, *9* (13), 3738–3743. https://doi.org/10.1021/acs.jpclett.8b01415.

(66) Qi, G.; Chu, Y.; Wang, Q.; Wang, X.; Li, Y.; Trébosc, J.; Lafon, O.; Xu, J.; Deng, F. Gem-Diol-Type Intermediate in the Activation of a Ketone on Sn-β Zeolite as Studied by Solid-State NMR Spectroscopy. *Angew. Chemie Int. Ed.* **2020**, *59* (44), 19532–19538. https://doi.org/https://doi.org/10.1002/anie.202005589.

(67) Wolf, P.; Valla, M.; Rossini, A. J.; Comas-Vives, A.; Núñez-Zarur, F.; Malaman, B.; Lesage, A.; Emsley, L.; Copéret, C.; Hermans, I. NMR Signatures of the Active Sites in Sn-β Zeolite. *Angew. Chemie Int. Ed.* **2014**, *53* (38), 10179–10183. https://doi.org/10.1002/anie.201403905.

(68) Wolf, P.; Liao, W.-C.; Ong, T.-C.; Valla, M.; Harris, J. W.; Gounder, R.; van der Graaff, W. N. P.; Pidko, E. A.; Hensen, E. J. M.; Ferrini, P.; Dijkmans, J.; Sels, B.; Hermans, I.; Copéret, C. Identifying Sn Site Heterogeneities Prevalent Among Sn-Beta Zeolites. *Helv. Chim. Acta* **2016**, *99* (12), 916–927. https://doi.org/10.1002/hlca.201600234.

(69) Wolf, P.; Valla, M.; Núñez-Zarur, F.; Comas-Vives, A.; Rossini, A. J.; Firth, C.; Kallas, H.;

Lesage, A.; Emsley, L.; Copéret, C.; Hermans, I. Correlating Synthetic Methods, Morphology, Atomic-Level Structure, and Catalytic Activity of Sn-β Catalysts. *ACS Catal.* **2016**, *6* (7), 4047–4063. https://doi.org/10.1021/acscatal.6b00114.

(70) Dijkmans, J.; Dusselier, M.; Gabriëls, D.; Houthoofd, K.; Magusin, P. C. M. M.; Huang, S.; Pontikes, Y.; Trekels, M.; Vantomme, A.; Giebeler, L.; Oswald, S.; Sels, B. F. Cooperative Catalysis for Multistep Biomass Conversion with Sn/Al Beta Zeolite. *ACS Catal.* **2015**, *5* (2), 928–940. https://doi.org/10.1021/cs501388e.

(71) Liu, L.; Lopez-Haro, M.; Lopes, C. W.; Meira, D. M.; Concepcion, P.; Calvino, J. J.; Corma, A. Atomic-Level Understanding on the Evolution Behavior of Subnanometric Pt and Sn Species during High-Temperature Treatments for Generation of Dense PtSn Clusters in Zeolites. *J. Catal.* **2020**, *391*, 11–24. https://doi.org/https://doi.org/10.1016/j.jcat.2020.07.035.

(72) Warnken, M.; Lázár, K.; Wark, M. Redox Behaviour of SnO2 Nanoparticles Encapsulated in the Pores of Zeolites towards Reductive Gas Atmospheres Studied by in Situ Diffuse Reflectance UV/Vis and Mössbauer Spectroscopy. *Phys. Chem. Chem. Phys.* **2001**, *3* (10), 1870–1876. https://doi.org/10.1039/B009045J.

(73) Morgan, K.; Goguet, A.; Hardacre, C. Metal Redispersion Strategies for Recycling of Supported Metal Catalysts: A Perspective. *ACS Catal.* **2015**, *5* (6), 3430–3445. https://doi.org/10.1021/acscatal.5b00535.

(74) Rice, R. W.; Chien, C. C. Simulation of Supported Iridium Catalyst Sintering and Redispersion. *J. Catal.* **1987**, *103* (1), 140–150. https://doi.org/https://doi.org/10.1016/0021-9517(87)90100-X.

(75) Newton, M. A. Dynamic Adsorbate/Reaction Induced Structural Change of Supported Metal Nanoparticles: Heterogeneous Catalysis and Beyond. *Chem. Soc. Rev.* **2008**, *37* (12), 2644–2657. https://doi.org/10.1039/B707746G.

(76) Douvalis, A. P.; Polymeros, A.; Bakas, T. IMSG09: A57Fe-119Sn Mössbauer Spectra Computer Fitting Program with Novel Interactive User Interface. *J. Phys. Conf. Ser.* **2010**, *217*, 12014. https://doi.org/10.1088/1742-6596/217/1/012014.

For Table of Contents Only

